JℲM PAPERS

Heat-transfer effects in compressible turbulent boundary layers – a regime diagram

Tobias Gibis[1],†, Luca Sciacovelli[2], Markus Kloker[1] and Christoph Wenzel[1],†

[1]Institute of Aerodynamics and Gas Dynamics, University of Stuttgart, 70569 Stuttgart, Germany
[2]DynFluid Laboratory, Arts et Métiers Institute of Technology, 151 bd. de l'Hôpital, 75013 Paris, France

As shown by Wenzel *et al.* (*J. Fluid Mech.*, vol. 930, 2022, A1), the Eckert number Ec defined using the difference between recovery temperature $\bar{T}_r$ and wall temperature $\bar{T}_w$ can be understood as a meaningful quantity to compare heat-transfer effects inside compressible turbulent boundary layers (for a calorically perfect gas), no matter whether these are caused by different Mach-number or wall-temperature conditions. While the named study deduced this comparative behaviour of Ec from an integral perspective in a strict sense, Cogo *et al.* (*J. Fluid Mech.*, vol. 974, 2023, A10) performed a systematic parameter study based on the previous findings to look at wall-normal profiles. They have shown that the diabatic parameter Θ, being equivalent to Ec, is capable of categorizing heat-transfer effects for cases at different Mach numbers, even to some extent for some of the wall-normal profiles. Building on this progress, the present paper provides a comprehensive classification of both existing and newly computed super- and hypersonic direct numerical simulation data at various wall temperature conditions into heated cases, adiabatic cases or weakly/moderately/strongly/quasi-incompressibly cooled cases. Hereby, the classification is largely based on the wall-normal position of the temperature peak occurring in cooled boundary-layer cases, which is one of the determining factors for the topological characteristics of diabatic boundary-layer profiles. Integrating high-enthalpy data into the analysis allowed us to confirm the reliability of the proposed classification also in more complex scenarios, where the calorically perfect gas assumption no longer applies and additional heat-transfer mechanisms come into play. While the Eckert number is shown to well characterize heat-transfer effects on most important temperature-related quantities for a wide range of Mach numbers and $\bar{T}_w/\bar{T}_r$ conditions, also the local Reynolds number Re_τ is shown to notably affect the strength of heat-transfer effects. Since both Ec and Re_τ can be determined in advance – or estimated to a reasonable extent – a key

† Email addresses for correspondence: tobias.gibis@iag.uni-stuttgart.de,
wenzel@iag.uni-stuttgart.de

advantage of the classification scheme is to allow for an effective *a priori* estimation of the extent to which heat-transfer effects are to be expected for a given compressible turbulent boundary-layer configuration.

Key words: compressible boundary layers, supersonic flow, turbulent boundary layers

---

1. Introduction

A major challenge in the investigation of compressible turbulent boundary layers (TBLs) lies in the larger number of relevant variables compared with incompressible TBLs. In addition to this extended parameter space, the complex interaction between different physical mechanisms makes the analysis and design of both experiments and simulations a challenging task. In particular, heat transfer inside the boundary layer affects the governing terms of the energy equation, resulting in significant influences on the wall-normal distributions of the most important terms of the governing equations. In the context of cooled walls, for instance, the turbulent heat flux $\bar{\rho}\widetilde{h''v''}$ becomes negative near the wall as a result of the positive temperature gradient in the near-wall region, and the turbulent fluctuations of the temperature $\sqrt{\overline{T'^2}}$ exhibit a tendency to form a second peak close to the wall; here $\bar{\rho}$ is mean density, and h'' and v'' fluctuating components of enthalpy and wall-normal velocity. Although most basic turbulence modelling assumptions, such as an almost constant turbulent Prandtl number Pr_t in the wall-normal direction, are surprisingly insensitive to heat-transfer effects in most cases, it is well known that some of the predictions made by the 'original' strong Reynolds analogy (SRA) of Morkovin (1962) for the temperature field of 'strongly' cooled cases do not hold. These modelling problems represent a large uncertainty in the prediction of boundary-layer behaviour, especially in hypersonic flows where wall heat transfer often takes precedence over skin friction as a design criterion. This particularly comes into play for the experimental investigation of hypersonic boundary layers, where the $\bar{T}_w/\bar{T}_r$ ratio is often very small due to wall temperatures $\bar{T}_w$ being far below the very high adiabatic (recovery) temperatures $\bar{T}_r$. For general compressible TBLs, a clear assessment of how strong the heat-transfer effects actually are is complicated because both the local Mach number – viscous heating increases with the square of the Mach number – and the wall-temperature condition contribute to the total heat transfer within the boundary layer. Consequently, easily tangible quantities like the temperature ratio between the boundary-layer edge and the wall $T_e/\bar{T}_w$ or between the wall and the adiabatic (recovery) temperature $\bar{T}_w/\bar{T}_r$ are not fully characterizing parameters. For instance, a temperature ratio of $\bar{T}_w/\bar{T}_r = 0.5$ represents significant cooling in subsonic cases but becomes far less significant at hypersonic Mach numbers, where viscous heating counteracts wall cooling.

1.1. *Objective of the study*

Significant progress has been made in the understanding of heat-transfer effects inside compressible TBLs in recent years. This applies both to a far-reaching insight into how severely the turbulent field of a compressible TBL can be affected by wall cooling at all, and to an improved understanding of how comparable heat-transfer effects within boundary layers are if cases with different Mach numbers and wall-temperature ratios are considered. Building on this progress, the main objective of this study is to build up a regime diagram, identifying the ranges in which heat-transfer effects cause a

clearly pronounced and substantially different behaviour in the wall-normal profiles of the temperature field. In order to have predictive capability, the classification scheme will be related to the friction Reynolds number $Re_\tau = \bar{\rho}_w u_\tau \delta_{99}/\bar{\mu}_w$, where $u_\tau = \sqrt{\tau_w/\bar{\rho}_w}$ is the friction velocity, δ_{99} the boundary-layer thickness, τ_w the wall-shear stress, ρ_w and μ_w wall-density and wall-viscosity, and the Eckert number

$$Ec = \frac{u_e^2}{\bar{h}_r - \bar{h}_w} \overset{c_p=\text{const.}}{=} \frac{u_e^2}{c_p(\bar{T}_r - \bar{T}_w)} = \frac{(\gamma - 1)M_e^2 T_e}{\bar{T}_r - \bar{T}_w}, \tag{1.1}$$

which can be understood as a meaningful quantity to compare heat-transfer effects inside compressible TBLs, no matter whether these are caused by different Mach-number or wall-temperature conditions; hereby $\bar{h}_r$ denotes the recovery enthalpy, for which no mean heat transfer is present at the wall, see § 4.1.2. Here u, T and M is the velocity, temperature and Mach number at the wall (subscript w), boundary-layer edge (subscript e) or its recovery value (subscript r), c_p is the specific heat and γ the specific heat ratio. By including both literature and newly generated direct numerical simulation (DNS) data with a specific sought-after behaviour, the advantages of this regime diagram are manifold: (i) firstly, the regime diagram enables an estimate of to what extent the wall-normal distributions of most important temperature-related variables are affected by heat-transfer effects arising from the interplay of the Mach number, wall temperature and Reynolds number. (ii) Secondly, as a direct consequence, the regime diagram allows a classification within which Ec- and Re-number ranges of a compressible TBL can be considered to be heated, adiabatic or weakly/moderately/strongly/quasi-incompressibly cooled. (iii) Thirdly, the diagram enables an estimate of the modelling errors (e.g. from the SRA) that can be expected for a given combination of Mach number, wall-temperature ratio and Reynolds number. (iv) Lastly, the results help us to assess to which degree Ec can be used as a comparative parameter for heat-transfer effects on wall-normal profiles at all. Therefore, this study can be seen as a logical follow-up to a large number of recent studies, bringing together different results and complementing the picture with new DNS data.

   The paper is structured as follows: firstly, a thorough literature review will be given in § 2, giving a summarizing overview of heat-transfer effects in compressible turbulent boundary layers reported in the literature. Secondly, the newly computed DNS data are introduced in § 3, before the regime diagram is introduced and discussed in §§ 4 and 5. Final conclusions are given in § 6.

1.2. *Terminology*

Throughout this study, the Mach-number-dependent heat generated within the boundary layer by the conversion of kinetic energy through reversible effects such as thermodynamic work plus the irreversible dissipation is referred to as 'viscous heating' (aerodynamic heating of the surface of super- and hypersonic vehicles). Besides, the heat transferred through the wall due to the temperature difference $\bar{T}_w - \bar{T}_r$ is referred to as 'wall heat transfer' (or 'wall-temperature effects'). Thus, the overall heat transferred within a boundary layer is the sum of viscous heating and wall heat transfer, and is simply referred to as 'heat transfer'.

   Reynolds (ensemble) averages are denoted by an overline $\bar{f}$, while Favre averages are denoted by a tilde $\tilde{f} = \overline{\rho f}/\bar{\rho}$; both are also spanwise averaged. The fluctuating components are denoted as $f' = f - \bar{f}$ and $f'' = f - \tilde{f}$ for Reynolds and Favre averaging, respectively.

Note that only quantities that actually fluctuate in time are indicated by an overline or tilde, so for example, edge values are indicated without an overline or tilde.

2. State of the art

In compressible TBLs, the local heat transfer and the thermal quantities are the result of the combined influence of the wall heat flux and wall-distant-dependent viscous heating

$$q \approx q_w + \bar{u}\tau_w, \qquad (2.1)$$

where q_w is the wall heat flux and τ_w the wall shear stress, see e.g. Gatski & Bonnet (2013) and Bradshaw & Huang (1995). The thermal quantities within a boundary layer are therefore determined by the balance between wall heat transfer and viscous heating. This becomes apparent most intuitively when considering cooled flows, where the wall heat transfer and viscous heating counteract each other; while q_w acts as a sink in the boundary layer's enthalpy balance, viscous heating acts as a source. As a consequence, the temperature profile exhibits a peak ($\partial \tilde{T}/\partial y = 0$) approximately at the wall-normal position where $\bar{u}\tau_w$ equals $q_w < 0$ (for cooling), or in other words, where the averaged streamwise velocity $\bar{u} = -q_w/\tau_w$. The consequences of this temperature peak are far reaching, as the change of sign in the temperature gradient largely affects the general topology of thermal quantities inside the compressible TBL. For example, the root mean square of the temperature fluctuations $\sqrt{\overline{T'^2}}$ becomes minimal in the region of the temperature maximum, and T' loses the known correlation with u' for adiabatic conditions. Remarkably, the presence of a temperature peak has no major consequences for the topology of the velocity field, which follows the same principles as known for incompressible cases with a constant stress layer forming near the wall. The resulting conclusion that density essentially affects the velocity field only passively has led to several outcomes, such as the velocity transformation, the semi-local scaling (which compensates for non-constant fluid properties in the wall-normal direction) and can be seen as the motivation for Morkovin's hypothesis. In contrast to adiabatic and heated cases, however, the 'inversed' correlation between u' and T' below the arising temperature peak makes the prediction of the temperature field notably more difficult for cooled cases, which has led to increased efforts in the past to improve its prediction by reformulating fundamental concepts like the SRA (see e.g. Gaviglio 1987; Huang, Coleman & Bradshaw 1995). In particular, the latest variant proposed by Zhang *et al.* (2014) has proven to be effective in predicting the diabatic temperature field by utilizing a generalized recovery enthalpy as a reference to the problem. Aside from using the similarity between the momentum and energy equations, which leads directly to a velocity–temperature relation of the form $T = f(u)$, Patel, Boersma & Pecnik (2017) and Chen *et al.* (2022) derived a temperature transformation using turbulent-viscosity models with the turbulent Prandtl number; this temperature transformation can be seen as an analogue to the well-known velocity transformation (see also Huang *et al.* 2023).

2.1. *Categorization of heat-transfer effects*

How intensely can a compressible TBL feel a given wall temperature? To answer this question, the mechanisms of wall heat transfer and viscous heating have to be weighted against each other. In the dimensionless total energy equation (enthalpy formulation)

$$\bar{\rho}\tilde{u}\frac{\partial \tilde{h}_0}{\partial x} + \bar{\rho}\tilde{v}\frac{\partial \tilde{h}_0}{\partial y} = \frac{Ec}{Re}\left[\frac{\partial}{\partial y}\left(\bar{\tau}_{xy}\bar{u} + \bar{\tau}_{yy}\bar{v}\right)\right] + \frac{Ec}{Re}\left[\frac{\partial}{\partial y}\left(\overline{\tau'_{xy}u'} + \overline{\tau'_{yy}v'} + \overline{\tau'_{zy}w'}\right)\right]$$

$$-\frac{\partial \bar{\rho}\widetilde{v''h''}}{\partial y} - \frac{\partial \bar{\rho}\widetilde{u''h''}}{\partial x} - \frac{Ec}{2}\left[\frac{\partial}{\partial y}\left(\bar{\rho}\widetilde{u''^2v''} + \bar{\rho}\widetilde{v''^3} + \bar{\rho}\widetilde{w''^2v''}\right)\right]$$

$$-Ec\left[\frac{\partial}{\partial y}\left(\tilde{u}\bar{\rho}\widetilde{u''v''} + \tilde{v}\bar{\rho}\widetilde{v''^2}\right)\right] - Ec\frac{\partial \tilde{u}\bar{\rho}\widetilde{u''^2}}{\partial x} - \frac{1}{RePr}\frac{\partial \bar{q}_y}{\partial y}, \quad (2.2)$$

where *Ec*, *Re* and *Pr* scale the physical importance of the individual terms with respect to each other. The value of *Ec* given in the special form of (1.1), resembles by definition the ratio between the effects of Mach number $M_e^2 = (\rho_e u_e^2)/(\gamma p_e)$, with *p* the pressure, to the effect of wall heat transfer. Note that this definition of *Ec* is based on $(\bar{h}_r - \bar{h}_w)$ as a characteristic enthalpy scale and the square of the boundary-layer-edge velocity u_e^2 as a characteristic scale for the kinetic energy (for a detailed reasoning of this choice, see Wenzel, Gibis & Kloker 2022). Furthermore, there is no explicit Mach-number dependence in the dimensionless numbers that scale (2.2), since M_e enters the equation solely through *Ec*. Thus, if *Re* is fixed for a problem with constant *Pr*, (2.2) suggests that the heat transfer within a boundary layer – and thus the manner in which a boundary layer feels the combined effects of the Mach number and wall heat transfer – is mainly determined by the local *Ec*. Note that the formulation of *Ec* in (1.1) is equivalent to the definition of the diabatic parameter $\Theta = (\bar{T}_w - T_e)/(\bar{T}_r - T_e)$ given in Zhang *et al.* (2014), as pointed out in Cogo *et al.* (2023). As shown in Wenzel *et al.* (2022) by mainly evaluating the wall-normal integrals of the respective terms of (2.2), the Eckert number (1.1) is able to predict the relative importance of the leading terms for a variety of diabatic DNS data at different Mach numbers, underlining the validity of *Ec* as a heat-transfer characterizing parameter. Wenzel *et al.* (2022) concluded that 'flow cases with the same *Ec* number are expected to exhibit the same integral behaviour and are thus physically comparable to each other, regardless of how this *Ec* number is achieved by adjusting the Mach number or the wall temperature'. Although these conclusions are mainly based on the integral perspective, the recent results by Cogo *et al.* (2023) suggest that also the wall-normal distribution itself, as well as the general flow structure, exhibits large similarities if cases at the same *Ec* are compared with each other. As an example, the wall-normal distribution of the temperature fluctuations $\sqrt{\overline{T'^2}}$ shows an almost identical course, including an arising inner peak for four cases with the same *Ec* but different Mach numbers and wall temperatures.

2.2. *A survey of heat-transfer effects in compressible turbulent boundary layers*

There are a large number of studies in the literature that have investigated the influence of Mach number, wall heat flux or Reynolds number on compressible TBLs with diabatic wall conditions. Being widely scattered across the parameter space, these studies outline the horizon of possible heat-transfer effects that may be encountered under diabatic conditions. In order to put these results into context and refer to known phenomena in the remainder of this study, a focused overview is given below.

2.2.1. *Flow structure*
In general, the flow structure is known to be strongly dependent on the Mach number, the wall temperature condition and the Reynolds number. In the case of wall cooling, for instance, the streaks within the boundary layer have been observed as tending to be longer and more coherent (see e.g. Morinishi, Tamano & Nakabayashi 2004;

Duan, Beekman & Martín 2010; Lagha *et al.* 2011). Xu, Wang & Chen (2023*b*) recently reported wave-like structures near the wall, which are quite pronounced in the case of strong wall cooling, but disappear in adiabatic cases. As a consequence of the broader parameter space of compressible TBLs, however, it is difficult to clearly assess whether the wall heat transfer or the Mach number is the dominant factor for the observed changes in the flow structure (Huang, Duan & Choudhari 2022), which always leaves some uncertainty in the interpretations of the results. In this respect, it is a notable conclusion of the recent study by Cogo *et al.* (2023) that the flow structure seems comparable for cases with the same *Ec* (or Θ) but different Mach number and heat-transfer conditions. Furthermore, it was shown by Cogo *et al.* (2023) that the mean temperature profile – and in particular the temperature maximum – has a strong impact on the thermal turbulent structures. For example, in the vicinity of the temperature maximum for the strongly cooled cases, the turbulent temperature structures lose the streaky pattern commonly observed in the adiabatic case.

2.2.2. *Temperature profile, turbulent heat flux and correlation coefficient*

Essentially, the most dominant changes in any turbulent thermal flow properties are directly due to variations in the wall-normal distribution of the temperature profile $\bar{T}$ (or $\tilde{T}$). For cooled conditions, the wall-normal temperature gradient $\partial \bar{T}/\partial y$ changes its sign compared with adiabatic conditions, becoming positive below the temperature peak $\partial \bar{T}/\partial y = 0$ for large regions near the wall (see e.g. Duan & Martín 2011; Shahab *et al.* 2011). In the spirit of Prandtl's mixing-length model, this causes the turbulent heat flux $\bar{\rho}\widetilde{v''h''}$ to also change its sign in the near-wall region where $\partial \bar{T}/\partial y$ is positive, while the Reynolds shear stress distribution $\bar{\rho}\widetilde{u''v''}$ remains negative throughout the boundary layer (Morinishi *et al.* 2004). General trends from the literature show that $\bar{\rho}\widetilde{v''h''}$ has a smaller magnitude for cooled boundary layers compared with adiabatic cases; moreover, higher-Mach-number cases tend to have a higher outer peak than lower-Mach-number cases (Fernholz, Finley & Mikulla 1981; Maeder, Adams & Kleiser 2001; Duan *et al.* 2010; Shahab *et al.* 2011). Another commonly used indicator of heat-transfer effects is the correlation coefficient $R_{u'T'} = \overline{u'T'}/(\sqrt{\overline{u'^2}}\sqrt{\overline{T'^2}})$ between u' and T'. For adiabatic boundary layers, $R_{u'T'}$ has been reported to be around -0.6 throughout most regions of the boundary layer (Guarini *et al.* 2000; Pirozzoli, Grasso & Gatski 2004; Pirozzoli & Bernardini 2011). For strongly cooled cases, $R_{u'T'}$ is found to be approximately $+1$ in the near-wall region, is nullified approximately at the wall-normal position where $\partial \bar{T}/\partial y = 0$ (Duan & Martín 2011) and closely follows the adiabatic trend above. This behaviour is frequently explained by using arguments based on gradient transport (Duan *et al.* 2010) or temperature variance production (Duan *et al.* 2010; Gatski & Bonnet 2013).

2.2.3. *Temperature fluctuation*

Although not appearing directly in the total-enthalpy equation (2.2), the temperature fluctuation $\sqrt{\overline{T'^2}}$ gives a visual access to intuitively assess the strength of heat transfer in compressible TBLs. Even if the reasons for its principal behaviour have already been sketched in the previous section, it is often the wall-normal distribution of $\sqrt{\overline{T'^2}}$ that is of particular value in the evaluation of heat-transfer effects. As an example, $\sqrt{\overline{T'^2}}$ can exhibit an additional peak in the region below the temperature peak $\partial \bar{T}/\partial y = 0$ for cold cases, which increases for higher cooling intensities while travelling further away from the wall

(see e.g. Tamano & Morinishi 2006; Duan & Martín 2011; Yu & Xu 2021; Cogo *et al.* 2023; Xu, Wang & Chen 2023*a*). Due to the strong correlation between the temperature gradient and the temperature fluctuations, the presence of this inner peak is usually only expected for 'very cold' wall conditions, and thus serves as a qualitative measure of how strongly a compressible TBL actually 'feels' a given wall temperature. Besides the existence of this inner peak, many studies report in general a decrease in temperature fluctuations with decreasing wall temperature (Shahab *et al.* 2011; Chu, Zhuang & Lu 2013). The reasoning is straightforward, the temperature fluctuations depend directly on the temperature gradient (Gatski & Bonnet 2013; Cogo *et al.* 2023) and thus can be included in Reynolds analogies that include the heat transfer (Gaviglio 1987; Huang *et al.* 1995; Zhang *et al.* 2014).

2.2.4. *Mach-number and Reynolds-number effects on the thermal boundary layer*

As outlined in § 2.1, the $\sqrt{\overline{T'^2}}$ distributions of cases with different Mach number but the same Ec and Re_τ show large similarities for wide regions across the boundary layer (Cogo *et al.* 2023). Nevertheless, although not explicitly appearing in (2.2), the Mach number can be assumed to also have a direct effect on the wall-normal distributions of important thermal flow variables. Moreover, the explicit appearance of *Re* in (2.2) suggests that also the Reynolds number severely affects heat-transfer effects in compressible TBLs. In reality, however, it is a challenging task to clearly assign pronounced changes in the wall-normal distributions to either the Reynolds number or the Mach number. While many studies have used the wall units to assess Reynolds-number dependencies, the semi-local scaling has gained in popularity in recent years, whereby boundary-layer parameters are scaled in the wall-normal direction with the local density and viscosity rather than using their wall values. Essentially, this scaling can be interpreted as a compressibility transformation of the wall-normal direction, as influences due to non-constant properties are 'eliminated' from the flow field by the utilization of local values (see e.g. Huang *et al.* 1995). Accordingly, also some of the recently proposed velocity transformations are based in some sense on the idea of semi-local scaling (Patel *et al.* 2015; Trettel & Larsson 2016; Griffin, Fu & Moin 2021), leading to notable improvements in the understanding of compressible TBLs. Based on a comparison in semi-local scaling, it has been observed that an increase in the Mach number can be usually associated with an increased scale separation if cases at same Re_τ are compared with each other (Cogo *et al.* 2023); similarly, cooling is assumed to decrease the scale separation (Huang *et al.* 2022). General observations have been that the effect of the wall heat transfer is often limited to the near-wall region, while a Mach-number change mostly affects the outer layer (Cogo *et al.* 2023). For higher Mach numbers, the outer layer usually shows higher fluctuating Mach numbers, as well as larger temperature and density variances, which are often traced back to the increased occurrence of shocklets at the turbulent–non-turbulent interface (Zhang, Duan & Choudhari 2018). For cases with additional heat transfer, cooled walls are associated with higher $M_\tau = u_\tau / \sqrt{\gamma \bar{p}_w / \bar{\rho}_w}$ values, suggesting that compressibility effects are more pronounced (Duan *et al.* 2010; Zhang *et al.* 2018). For the $\sqrt{\overline{T'^2}}$ distributions at very cold wall conditions, Xu *et al.* (2023*a*) reported that increasing the Reynolds number slightly increases the intensity of the arising near-wall peak. Simultaneously, the $\sqrt{\overline{T'^2}}$ distribution in the outer layer near the boundary-layer edge has been found to decrease as *Re* and *M* increase. Further, it was noted that $\sqrt{\overline{T'^2}}$ has stronger positive than negative magnitudes near the boundary-layer edge.

2.2.5. *Pushing to hypersonics – high-enthalpy effects*

High-enthalpy effects refer to a wide class of physical processes caused by the large temperature values within the boundary layer of vehicles travelling at hypersonic speeds. Their presence entails a variation in the distribution of the internal energy at the molecular scale, and the generation of additional energy transfer pathways that could potentially alter the classical ideal-gas picture, whereby the heat flux is solely driven by molecular heat conduction. At high temperatures, oxygen and nitrogen molecules can be subject to vibrational excitation and chemical dissociation processes, leading to an increase of the thermal capacities and a modification of the local gas mixture composition. Due to the newly available modes for storing energy and the endothermic nature of the reactions, the net effect is an overall reduction of $\bar{T}$ and $\sqrt{\overline{T'^2}}$ values within the boundary layer (see e.g. Duan & Martín 2011; Passiatore *et al.* 2021; Liu *et al.* 2023). Part of the energy drained by molecular dissociation can be regained by atom recombination, which can be significant in the viscous sublayer (Di Renzo & Urzay 2021). The relative decrease of the thermal conduction contribution to the heat transfer – due to the reduced temperature gradients – can be counterbalanced by the increase of the thermal diffusion component, driven by the species' concentration gradients. A major difference with respect to low-enthalpy flows concerns indeed the role of gas–surface interactions in the heat-transfer rates. Catalytic surfaces strongly enhance the heat-flux levels at the wall, such that the catalytic heat flux can be a large portion of the total heat flux when the flow is significantly dissociated (Duan & Martín 2011). Furthermore, ablative materials lead to further energy drain through chemical reactions, sublimation and gas blowing processes (Candler 2019). At higher enthalpies and lower pressures, vibrational and rotranslational modes might reequilibrate slowly, resulting in a thermal non-equilibrium state. Under such a regime, Passiatore *et al.* (2022) reported that the vibrational and rotranslational temperatures exhibit different wall-normal profiles, therefore affecting the total heat-transfer distribution throughout the boundary layer. The turbulent heat flux $\bar{\rho}\widetilde{v''h''}$ is also shown to be sensitive to high-enthalpy conditions, mainly because of the turbulent species' transport contribution (Li *et al.* 2022). Despite the intricate behaviour of the processes involved, generalized enthalpy-based Reynolds analogies (Duan & Martín 2011; Zhang *et al.* 2014) have been shown to perform reasonably well, even for high-enthalpy flows.

3. Simulation details

For this study, five DNS of compressible zero-pressure-gradient TBLs at a Mach number $M_e = 2.0$ are computed: a heated one, an adiabatic one and three cooled ones. As will be elaborated in the following in more detail, the specific wall temperature of each cooled case has been set to achieve what will later be denoted as weakly, moderately and strongly cooled cases, see tables 1 and 2 for details. All five computations are performed using the compressible high-order in-house DNS code NS3D, with the principal numerical set-ups closely following Wenzel *et al.* (2019). A perfect gas with a constant $\gamma = c_p/c_v = 1.4$ and a constant Prandtl number $Pr = 0.71$ is assumed. The temperature dependency of the viscosity and thermal conductivity is modelled by Sutherland's law and the linear law below the Sutherland temperature. The equations are solved on a block-structured Cartesian grid spanning a rectangular integration domain. For spatial discretization, sixth-order subdomain-compact finite differences (FDs) in all three directions are used, see Keller & Kloker (2013); for time stepping, the classical fourth-order Runge–Kutta scheme is employed, coupled with alternating forward- and backward-biased FDs for the convective first derivatives, see Kloker (1997) and Babucke (2009). The wall temperature

995 A14-8

	Case	$-1/Ec$	Θ	$\bar{T}_w/\bar{T}_r$	Re_θ	$Re_{\delta_{99}}$	Re_τ
(1)	cZPG$_h$	0.357	1.79	1.33	2199–6669	26 265–79 978	335–883
(2)	cZPG$_{ad}$	0.0	1.0	1.0	2157–4349	23 272–46 731	439–804
(3)	cZPG$_{wc}$	−0.224	0.5	0.79	1107–3481	11 235–34 607	314–830
(4)	cZPG$_{mc}$	−0.434	0.03	0.6	895–2593	8433–23 768	367–898
(5)	cZPG$_{sc}$	−0.686	−0.53	0.36	705–1564	6122–13 064	549–1063

Table 1. Summary of the simulation parameters for the cases simulated in this study. Quantities are given at the beginning and end of the region of interest.

	Case	$c_f \times 10^{-3}$	c_h	$(L_x \times L_y \times L_z)/\delta_{99,0}$	$L_{x,roi}/\delta_{99,0}$	$N_x \times N_y \times N_z$
(1)	cZPG$_h$	2.40–1.80	4.12–4.02	$2040 \times 85 \times 90$	400	$17\,408 \times 408 \times 1152$
(2)	cZPG$_{ad}$	2.66–2.21	—	$1115 \times 50 \times 45$	200	$14\,080 \times 440 \times 1120$
(3)	cZPG$_{wc}$	3.35–2.47	1.99–1.44	$830 \times 40 \times 52$	150	$9216 \times 592 \times 1216$
(4)	cZPG$_{mc}$	3.77–2.85	2.22–1.67	$530 \times 35 \times 30$	100	$11\,008 \times 520 \times 1120$
(5)	cZPG$_{sc}$	4.22–3.47	2.48–2.04	$245 \times 16 \times 20$	60	$10\,496 \times 592 \times 1152$

Table 2. Summary of numerical set-up information for the compressible TBLs simulated in this study. The parameters are given for the beginning (given by $L_{x,roi}$) and the end of the region of interest.

for all diabatic cases is prescribed as an isothermal no-slip condition; for the adiabatic case, enforcing $(\partial T/\partial y)_w = 0$ allows us to obtain the true recovery factor. For both diabatic and adiabatic cases the wall pressure is computed according to $(\partial p/\partial y)_w = 0$ using an optimized fifth-order stencil like for $(\partial T/\partial y)_w = 0$. A digital filtering technique was used for the inflow condition (see Wenzel *et al.* 2018, 2019) with the modification of using the relation of Zhang *et al.* (2014) for the temperature fluctuations to improve the stability of the simulations at the inlet for moderately and strongly cooled cases. A maximum grid spacing of $\Delta y_w^+ \lessapprox 0.5$–0.6, $\Delta x_w^+ \lessapprox 8$, $\Delta z_w^+ \lessapprox 4$ at the wall and $\Delta y^+ \lessapprox 4$ in the wall-normal direction away from the wall was targeted, see table 2 for the grid dimensions. Data averaging is performed both in time and spanwise direction and only started after the flow has passed the whole simulation domain at least twice. Consistently for all cases, time averages were performed for longer than a flow-through time corresponding to approximately $\Delta t u_e/\delta_{99} = 250$, with δ_{99} the local boundary-layer thickness. Note that the beginning of the region of interest $L_{x,roi}$ (corresponding to the beginning of the post-processed region) is between 60 and 400 inlet boundary-layer thicknesses $\delta_{99,0}$ away from the inlet plane in all simulations. It is therefore far enough downstream to not be adversely affected by the inlet boundary condition, see table 2 and Ceci *et al.* (2022).

4. Classification of heat-transfer effects

As summarized in § 2.2, specific features can be observed in the thermal properties of compressible TBLs which can be clearly associated with the intensity of heat-transfer effects within the boundary layer. Thus, assuming that Ec can classify heat-transfer effects to a considerable degree at a given Re, it is possible to provide a physical feature-based Ec categorization assessing the strength of heat-transfer effects for a given Mach number and wall temperature. In this section, the basic behaviour of the Eckert number is first discussed in § 4.1 as a function of $\bar{T}_w/\bar{T}_r$ and M_e, and the literature DNS data are arranged in the parameter space. Afterwards, the identification of heat-transfer regimes is established in

§ 4.2, which is mainly based on the wall-normal position of the temperature peak ($\partial\tilde{T}/\partial y$). In the remaining §§ 4.3, 4.4 and 4.5, the influences of Reynolds number, Mach number and high-enthalpy effects on the classification are discussed.

4.1. *Introduction of the regime diagram*

In figure 1, both the Eckert number Ec (left ordinate) and the diabatic parameter Θ (right ordinate) are depicted as function of the boundary-layer-edge Mach number M_e (abscissa) and the commonly used wall-to-recovery-temperature ratio $\bar{T}_w/\bar{T}_r$ (lines). In line with Wenzel *et al.* (2022), the lines of constant $\bar{T}_w/\bar{T}_r$ are computed for every M_e and Ec under the assumption of $\bar{T}_r/T_e = 1 + r(\gamma - 1)/2M_e^2$, where the recovery factor has been set to $r = Pr^{1/3}$ and $\gamma = 1.4$ for all cases. For cases with $\gamma \neq 1.4$, the $\bar{T}_w/\bar{T}_r$ lines differ at low M_e but coincide with the lines for $\gamma = 1.4$ at hypersonic Mach numbers, where the lines become independent of γ

$$\lim_{M_e \to \infty} (-1/Ec) = \lim_{M_e \to \infty} \left(\frac{\bar{T}_w}{\bar{T}_r} - 1\right) \frac{1 + r\dfrac{\gamma - 1}{2}M_e^2}{(\gamma - 1)M_e^2} = \left(\frac{\bar{T}_w}{\bar{T}_r} - 1\right)\frac{r}{2}. \quad (4.1)$$

To illustrate the influence of a γ variation, only the $\bar{T}_w/\bar{T}_r = 0$ line is shown for an exemplary value of $\gamma = 1.3$, which is representative for the high-enthalpy cases by Di Renzo & Urzay (2021) and Passiatore *et al.* (2022). Note that the line for $\bar{T}_w/\bar{T}_r = 0$ is indicative of the expected deviations for all $\bar{T}_w/\bar{T}_r$ lines, which are omitted for the sake of clarity. It is further noted that, for high-enthalpy cases, the location in the Ec-space should strictly speaking rather be based on the $\bar{h}_w/\bar{h}_r$ ratio instead of $\bar{T}_w/\bar{T}_r$. In contrast to Wenzel *et al.* (2022), the Ec value on the left ordinate in figure 1 is defined by its negative reciprocal $-1/Ec$ due to three reasons: (i) while Ec becomes infinite for adiabatic cases, its reciprocal becomes zero, representing thus a somewhat more intuitive choice. (ii) By forming the reciprocal of Ec, the parameter space for strongly cooled or heated cases is further fanned out, which enables a more clear distinction between the individual cases. (iii) With the negative sign, $-1/Ec$ is negative for cooled cases and positive for heated cases, which is also somewhat more intuitive compared with the opposite case. Thus, cases at adiabatic wall conditions ($\bar{T}_w/\bar{T}_r = 1$) are characterized by $-1/Ec = 0$ in figure 1; cases in the upper half of figure 1 are cases with a heated/heating wall ($\bar{T}_w/\bar{T}_r > 1$), while the lower half of the figure displays cases with a cooled/cooling wall ($\bar{T}_w/\bar{T}_r < 1$). Implied by the course of the coloured lines for constant $\bar{T}_w/\bar{T}_r$, both an increase in heating and cooling (increase and decrease in $\bar{T}_w/\bar{T}_r$, respectively) as well as a decrease in M_e result in an increase in the absolute value of $-1/Ec$, which is equivalent to the fact that heat-transfer effects are more pronounced in the corresponding boundary layers. Consequently, with increasing Mach number M_e, an increasingly strong heating or cooling $|\bar{T}_r - \bar{T}_w|$ is necessary to achieve large absolute values for $-1/Ec$. In addition, as implied by the almost constant course of the lines for constant $\bar{T}_w/\bar{T}_r$ at higher Mach numbers, the influence of M_e on $-1/Ec$ is shown to decrease drastically for high hypersonic Mach numbers, leaving the value of $-1/Ec$ almost exclusively a function of $\bar{T}_w/\bar{T}_r$ only.

4.1.1. *Physical interpretation*

Essentially, all of the aforementioned trends are the direct consequence of the Ec definition chosen. In its present formulation (1.1), the Eckert number is a measure of the contribution of kinetic energy difference to wall heat transfer. For a fluid like air, this is similar to
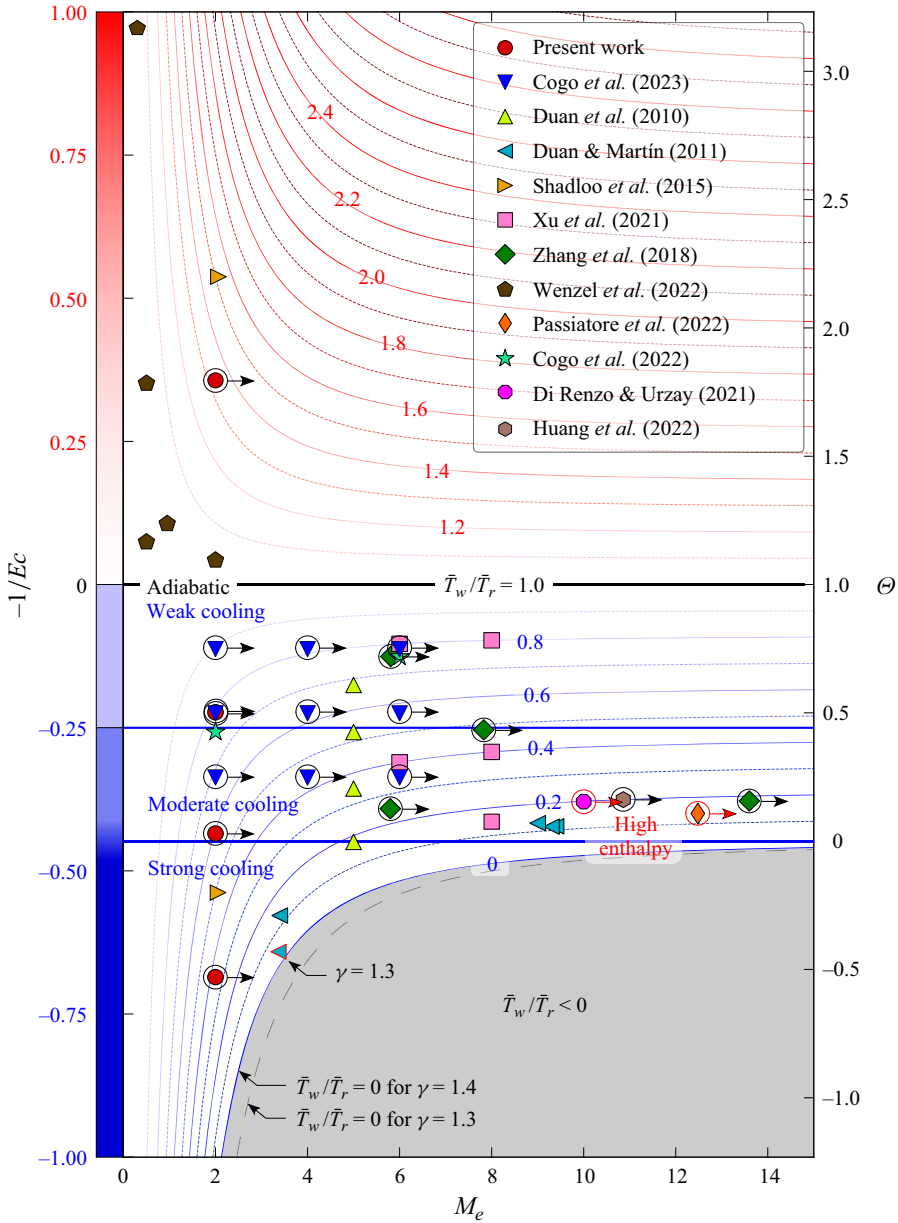
Figure 1. Collection of compressible DNSs at different Mach numbers M_e plotted over $-1/Ec$ (left axis) or equivalently over the diabatic parameter Θ (right axis). For conversion, the values of $-1/Ec$ resulting from a given $\bar{T}_w/\bar{T}_r$ are also plotted over M_e as red and blue curved lines. The two horizontal blue lines denote the approximate $-1/Ec$ at which the regime change occurs for recent DNS with a Reynolds number of $400 \lesssim Re_\tau \lesssim 1200$. The data points with a circle denote cases plotted in figure 2.

the contribution of viscous heating to wall heat transfer where the Brinkman number $Br = EcPr$ is of the same order of magnitude. The course of the $\bar{T}_w/\bar{T}_r$ curves in figure 1 thus merely reflects the fact that a boundary layer at low Mach numbers feels a given $\bar{T}_w/\bar{T}_r$ much more intensely than a boundary layer at higher Mach numbers, where viscous heating comes increasingly into play as a dominant energy transfer mechanism.

This becomes particularly evident by considering cooled cases with a (hypothetical) maximum cooling intensity of $\bar{T}_w/\bar{T}_r = 0$. Due to the counteracting effects of wall cooling (sink in the enthalpy balance) and viscous heating (source in the enthalpy balance), the curve for $\bar{T}_w/\bar{T}_r = 0$ represents a natural limit for each corresponding Mach number below which no further decrease in $-1/Ec$ is possible. Essentially, this limit value simply states that there is a minimum value in $-1/Ec$ for which no more heat can be extracted by the wall cooling than is simultaneously made available by heating within the boundary layer. Accordingly, the trend of $\bar{T}_w/\bar{T}_r = 0$ takes on great importance, as it provides an indication of how strongly a boundary layer can be influenced by heat-transfer effects at a specific Mach number at all. It is indicated by the course of $\bar{T}_w/\bar{T}_r = 0$ in figure 1, for instance, that a supersonic boundary layer at $M_e = 2$ and $\bar{T}_w/\bar{T}_r = 0.5$ will show heat-transfer effects in some of its thermal properties that are actually impossible to physically reproduce at hypersonic Mach numbers, even for the strongest possible cooling ($\bar{T}_w/\bar{T}_r = 0$). Moreover, the minimum achievable values (at $\bar{T}_w/\bar{T}_r = 0$) for $-1/Ec$ and Θ are well-defined values in the hypersonic limit; that is, $\lim_{M_e \to \infty}(-1/Ec) = -r/2$ and $\lim_{M_e \to \infty}(\Theta) = 0$, respectively, compare (4.1). The existence of this hypersonic limit is a consequence of the fact that, in hypersonic flows, the internal energy of the free stream is negligible compared with its kinetic energy, so that basically all of the heat transferred through the wall stems from viscous heating within the boundary layer.

4.1.2. *Introduction of the DNS data in the regime diagram*

To get a first overview of the DNS data considered in the following, all data summarized in table 3 are plotted as symbols in figure 1. Note that the recovery enthalpy $\bar{h}_r$ for the hypersonic cases with calorically non-perfect gases ($\bar{h}_r \neq c_p \bar{T}_r$) is estimated by $\bar{h}_r = h_e + (r/2)u_e^2$, where a recovery factor of $r = 0.9$ is assumed, consistent with Duan & Martín (2011) and Passiatore *et al.* (2022). From figure 1, the vast majority of cases was calculated for cooled-wall conditions, and only a few cases with low Mach number for heated-wall conditions. For the cooled-wall cases, a large number of cases lie in the range $0 > -1/Ec \gtrsim -0.25$, which will be referred to later as the weakly cooled regime; a comparable amount lie between $-0.25 \gtrsim -1/Ec \gtrsim -0.45$, which will later be referred to as the moderately cooled regime; and only a few data, especially at lower Mach numbers, lie in the range of $-1/Ec \gtrsim -0.45$, which will later be referred to as the strongly cooled regime. When considering the temperature ratios $\bar{T}_w/\bar{T}_r$, the cases of Duan *et al.* (2010), Duan & Martín (2011), Zhang *et al.* (2018), Di Renzo & Urzay (2021), Xu *et al.* (2021a), Huang *et al.* (2022) and Passiatore *et al.* (2022) are noteworthy, with values for $\bar{T}_w/\bar{T}_r$ being very close to the cooling limit of $\bar{T}_w/\bar{T}_r = 0$ for the respective selected Mach numbers. However, the case with the lowest value for $-1/Ec$ – and thus the case that exhibits the strongest heat-transfer effects in the following – is the newly computed case with $M_e = 2$ and $\bar{T}_w/\bar{T}_r = 0.36$, which was designed especially for this purpose, see § 3 for details. Further emphasis should be given to the data from Cogo *et al.* (2023), where a 3 by 3 array of data evenly distributed in the M_e and Ec space was generated. This data set is the most appropriate when Mach-number effects are to be identified for 'comparable' cases with the same $-1/Ec$ and Re_τ.

4.2. *Classification of heat-transfer effects*

Following the introduction of the regime diagram in the previous section, the objective of this section is to present a subdivision of the parameter space for which the overall effect

	Case	$-1/Ec$	Θ	$\bar{T}_w/\bar{T}_r$	M_e	Re_τ	$M_\tau \times 1000$	$B_q \times 1000$
(1)	Present	0.357	1.79	1.33	2.0	335–882	69.5–60.2	$-15--13$
		0.0	1.0	1.0	2.0	438–804	73.0–66.7	0.0
		−0.224	0.50	0.79	2.0	314–830	81.8–70.3	14.6–12.4
		−0.434	0.03	0.6	2.0	366–897	86.6–75.5	36.2–31.3
		−0.686	−0.53	0.36	2.0	549–1063	92.5–83.8	77.2–69.8
(2)	Cogo *et al.* (2023)	−0.336	0.25	0.69	2.0	443	82.5	22.9
		−0.224	0.5	0.79	2.0	443	79.6	13.4
		−0.112	0.75	0.9	2.0	443	77.2	5.7
		0.0	1.0	1.0	2.0	443	74.7	0.0
		−0.336	0.25	0.44	4.0	443	132.7	61.0
		−0.224	0.5	0.63	4.0	443	122.0	30.7
		−0.112	0.75	0.81	4.0	443	113.7	11.7
		−0.336	0.25	0.25	6.0	443	159.3	89.0
		−0.224	0.5	0.5	6.0	443	140.8	40.5
		−0.112	0.75	0.75	6.0	443	129.9	14.9
		0.0	1.0	1.0	6.0	443	121.1	0.0
(2)	Cogo *et al.* (2022)	−0.26	0.42	0.76	2.0	340–620	—	$\approx$160
		−0.26	0.42	0.76	2.0	1240–2300	$\approx$65.6	$\approx$190
		−0.125	0.72	0.76	5.86	290–520	—	$\approx$130
		−0.125	0.72	0.76	5.86	1080–1953	$\approx$108.2	$\approx$140
(3)	Duan & Martín (2011)	−0.641	−0.29	0.13	3.4	906	—	—
		−0.641	−0.29	0.13	3.4	910	—	—
		−0.422	0.08	0.13	9.4	786	—	—
		−0.423	0.07	0.13	9.3	741	—	—
		−0.551	−0.23	0.17	3.4	938	—	—
		−0.422	0.06	0.12	9.0	906	—	—
(3)	Duan *et al.* (2010)	−0.450	0.00	0.18	4.97	798.1	—	—
		−0.357	0.20	0.35	4.97	624.7	—	—
		−0.258	0.42	0.53	4.97	522.2	—	—
		−0.176	0.61	0.68	4.97	433.8	—	—
(7)	Zhang *et al.* (2018)	−0.396	0.13	0.25	5.84	450	170	140
		−0.125	0.72	0.76	5.86	453	130	20
		−0.254	0.43	0.48	7.87	480	150	60
		−0.378	0.16	0.18	13.64	646	190	190
		0.0	1.0	1.0	2.5	510	80	0.0
(8)	Shadloo, Hadjadj & Hussain (2015)	0.536	2.21	1.5	2.0	350	64.1	—
		−0.536	−0.19	0.5	2.0	550	85.8	—
(10)	Xu *et al.* (2021*b*)	−0.311	0.31	0.4	6.0	1615	—	—
		−0.104	0.77	0.8	6.0	688	—	—
		−0.414	0.08	0.15	8.0	2444	—	—
		−0.292	0.35	0.4	8.0	887	—	—
		−0.097	0.78	0.8	8.0	1386	—	—
(11)	Wenzel *et al.* (2022)	0.97	3.17	1.03	0.3	274–726	—	—
		0.08	1.17	1.01	0.5	271–731	—	—
		0.35	1.79	1.03	0.5	263–714	—	—
		0.11	1.24	1.03	0.95	228–612	—	—
		0.04	1.10	1.04	2.0	146–478	—	—
(12)	Di Renzo & Urzay (2021)	≈-0.43	$\approx$0.05	$\approx$0.1	10	1104	230	260
(13)	Passiatore *et al.* (2022)	≈-0.4	$\approx$0.11	$\approx$0.14	12.48	1128	210	240
(14)	Huang *et al.* (2022)	−0.375	0.16	0.2	10.9	772–1172	182–167	163–148

Table 3. Summary of parameters from the DNS datasets used in this study. The Eckert number $Ec = u_e^2/(\bar{h}_w - \bar{h}_r)$, the diabatic parameter $\Theta = (\bar{T}_w - T_e)/(\bar{T}_r - T_e)$, the friction Reynolds number $Re_\tau = \bar{\rho}_w u_\tau \delta_{99}/\bar{\mu}_w$, the friction Mach number $M_\tau = u_\tau/\bar{a}_w$ where $\bar{a}_w$ is the speed of sound at the wall, the inner-scaled heat transfer $B_q = q_w/(\bar{\rho}_w \bar{h}_w u_\tau)$. Note: for (13) the rotranslational dimensionless heat flux is given.

of heat transfer on the compressible TBL can be expected to be significantly different. In other words, it is the objective to identify physical feature-based regimes, for which heat-transfer effects can be denoted to be weak, moderate or strong. To allow for an assessment of how strongly the respective cases are influenced by heat-transfer effects, the wall-normal distributions of the most important temperature-related quantities is given in figure 2, as far as available for the data under consideration. Given quantities are: (i) the temperature fluctuations $\sqrt{\widetilde{T'^2}}$ as a quantity where the strength of heat transfer becomes most tangible, (ii) the premultiplied wall-normal temperature gradient $y\partial\tilde{T}/\partial y$ as the most representative quantity and (iii) the turbulent heat flux $\bar{\rho}\widetilde{h''v''}$ as the most relevant quantity in the energy equation for turbulence modelling. All data are labelled by their respective values of $-1/Ec$ and Mach number in brackets (M_e); both for the presents data in red and the data by Huang *et al.* (2022) in brown, data at two Reynolds numbers are plotted to evaluate the trend of increasing Reynolds number in § 4.3. All wall-normal distributions are plotted in semi-local scaling with $y^* = (\bar{\rho}\sqrt{\tau_w/\bar{\rho}}y)/\bar{\mu}$ and $u_\tau^* = \sqrt{\tau_w/\bar{\rho}}$, which has been found to be superior in the context of the regime diagram than plotting in wall units (see Appendix A for a variant in wall units). Another possibility would be to use the sub- and buffer-layer definitions used in the multilayer scale definition of Wu *et al.* (2017). Note that the proposed classification is, strictly speaking, limited to cases with Prandtl number $Pr = O(1)$ and additional regimes may occur for cases with $Pr \neq O(1)$.

Comments: the temperature fluctuations were plotted as Reynolds-averaged fluctuations, as the corresponding Favre-averaged values are only available in a few data sets. The difference is typically insignificant, see e.g. Huang *et al.* (1995). In figure 2, the temperature in $\partial\tilde{T}/\partial y$ is represented in wall units, $\tilde{T}^+ = \tilde{T}/(\gamma\tilde{T}_wM_\tau)$, as a simple semi-local scaling attempt similar to $\tilde{T}^* = \tilde{T}/(\gamma\tilde{T}M_\tau^*)$ that results in a nearly constant function; nevertheless, to account for density variations in the wall-normal direction, the semi-local part with $\bar{\rho}/\bar{\rho}_w$ was added as a multiplication outside the derivative. Besides, $\bar{\rho}\widetilde{h''v''}$ is normalized with $\bar{\rho}u_\tau^{*3}$, which is motivated by the general result of Gibis *et al.* (2019) that the energy scale should be proportional to the square of the velocity scale. Other potential choices either involve q_w, thus being not valid for adiabatic cases, or make use of scaling variables similar to B_q, which are not able to scale all cases to the same order of magnitude (compare B_q in table 3). Lastly, for the data by Di Renzo & Urzay (2021), the distribution of $\bar{\rho}\widetilde{h''v''}$ is estimated from $\bar{\rho}\widetilde{T''v''}$ with a local c_p computed via NASA polynomials for air (McBride, Zehe & Gordon 2002).

4.2.1. *Adiabatic conditions*

As a reference point for all subsequent discussions, the adiabatic cases shown in the second row of figure 2 are introduced first. For adiabatic conditions, the temperature gradient in panel (*b*ii) is caused exclusively by viscous heating. Since no heat is transported through the wall, the temperature at the adiabatic wall is the highest within the boundary layer, so the temperature gradient is strictly negative throughout the entire boundary layer. Accordingly, the turbulent heat flux $\bar{\rho}\widetilde{h''v''}$ remains strictly positive in panel (*b*iii). Furthermore, as both $\partial\tilde{T}/\partial y$ and $\partial\tilde{u}/\partial y$ have the same qualitative two-peak structure, the course of $\bar{\rho}\widetilde{h''v''}$ qualitatively follows that of the turbulent shear stress $\bar{\rho}\widetilde{u''v''}$, as implied by the nearly constant course of the turbulent Prandtl number $Pr_t = (-\bar{\rho}\widetilde{u''v''})/(-\bar{\rho}\widetilde{T''v''})(\partial\tilde{T}/\partial y)/(\partial\tilde{u}/\partial y)$. Similarly, the turbulent temperature fluctuations
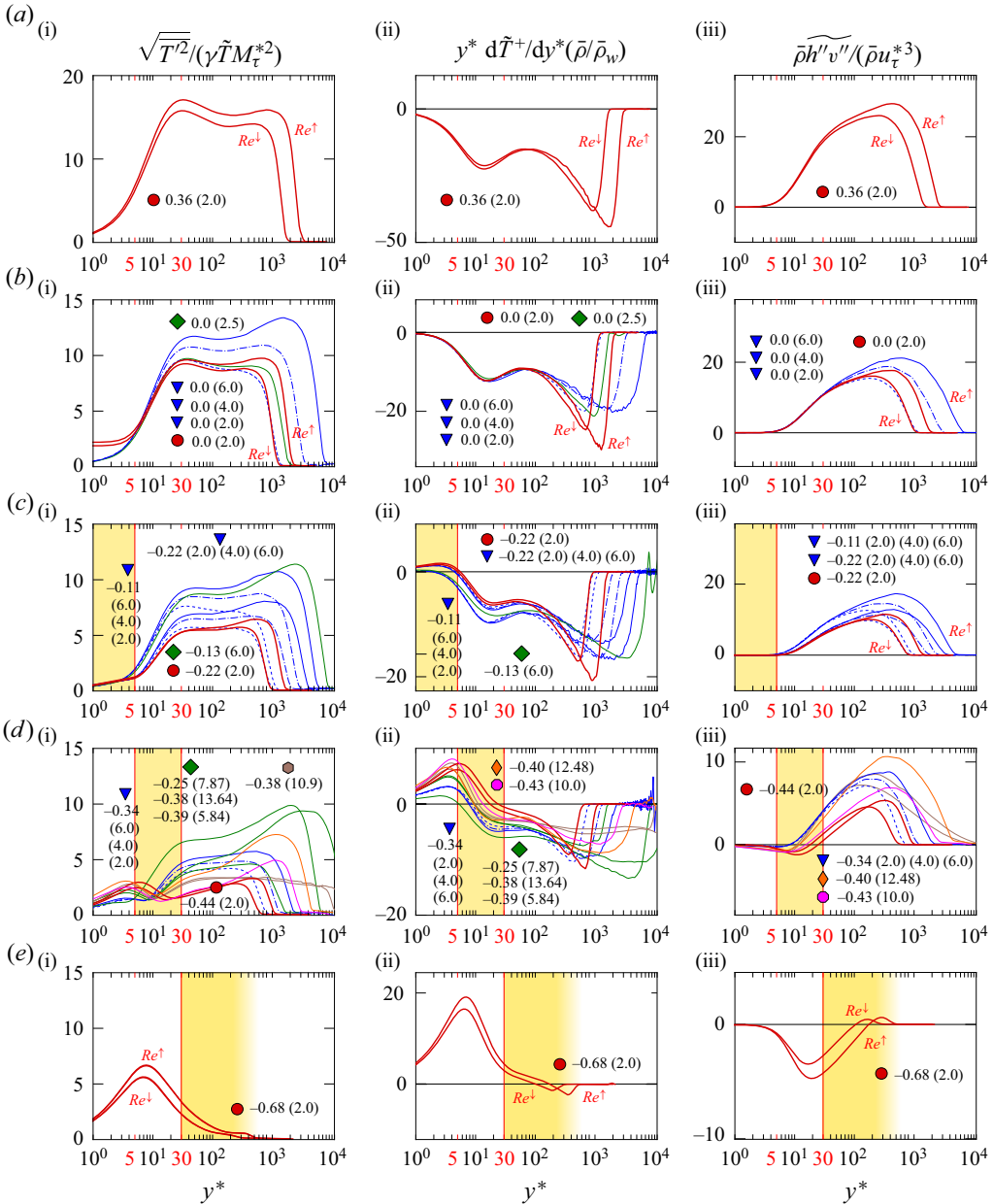
995 A14-14

Figure 2. Plot of the semi-locally scaled temperature fluctuation (labelled as (i) in the left column), the pre-multiplied temperature gradient (labelled as (ii) in the middle column) and the normalized turbulent heat flux (labelled as (iii) in the right column). The rows, from top to bottom, correspond to the regimes: (a) heated, (b) adiabatic, (c) weakly cooled, (d) moderately cooled and (e) strongly cooled. Each data point is identified by its respective value of $-1/Ec$ and Mach number in brackets (M_e). The legend in figure 1 includes the references for the line colours and symbols.

in panel (b i) show minima and maxima at locations where the magnitude of $\partial \tilde{T}/\partial y$ is small and large, respectively.

Although discussed in more detail later, the effects of Reynolds number and Mach number on the curves shown can be estimated by comparing the present data with the

995 A14-15

data from Cogo *et al.* (2023). While present data in red are evaluated at the same M_e but at different Re_τ, the data in blue are evaluated at different M_e but same Re_τ. Note that the present data are the only ones computed under truly adiabatic conditions, implying that temperature fluctuations in panel (*b*,i) do not disappear at the wall as they do in isothermal, pseudo-adiabatic boundary conditions. In the chosen semi-local representation, increasing both the Mach number and the Reynolds number pushes δ^*_{99} further out on the abscissa; the Mach number implicitly via an increase in the wall-normal density variation, the Reynolds number directly via an increase in the boundary-layer thickness. On the ordinate, an increase in both the Mach and Reynolds numbers increases only slightly the magnitude of the inner peak of $\sqrt{\overline{T'^2}}$, and more intensely the outer peak, see e.g. Cogo *et al.* (2023) for more details. Consequently, in a semi-local scaling, an increase in Mach number acts largely analogously to an increase in Reynolds number, which directly resembles the physical spirit of a heated boundary layer.

4.2.2. *Heating conditions*

For the heated cases in panels (*a* i)–(*a* iii), the viscous heating is accompanied by wall heat transfer. As both mechanisms act as a source, the heat has to be transported away from the wall, similar to the adiabatic cases. Thus, the temperature gradient $\partial \tilde{T}/\partial y$ is strictly negative throughout the boundary layer. Consequently, the distributions of the turbulent heat flux in panel (*a* i) and the temperature fluctuations in panel (*a* iii) follow the same reasoning as discussed in §4.2.1 for adiabatic cases, essentially being only increased in magnitude due to a steeper temperature gradient. In terms of the flow structure, the increased wall temperature leads to an increased scale separation analogous to cases at higher Mach numbers, as flow structures in the outer layer are smaller compared with an adiabatic case, see also figure 7. However, since no significant change in the course of essential thermal flow field variables is to be expected with an increase of $-1/Ec$, a subdivision of the heated cases into sub-regimes has no additional value. For these cases, only the specification of $-1/Ec$ and Re (or Θ and Re) is decisive as a measure of the strength of the heat transfer within a boundary layer.

4.2.3. *Weak cooling conditions*

Under cooling conditions, the wall heat transfer counteracts the effect of viscous heating, see §2.2.2. As a result, the temperature gradient $\partial \tilde{T}/\partial y$ becomes positive at the wall, causing the temperature profile to develop a temperature peak in the near-wall region. As shown in figure 2(*c* i–*c* iii), the term 'weakly cooled' is chosen for cases where the peak of the temperature field – and thus the root of $\partial \tilde{T}/\partial y = 0$ in panel (*c* ii) – is still in the viscous sublayer at $y^* \lesssim 5$, and thus in a region where the boundary-layer behaviour is dominated by viscosity rather than turbulence. Consequently, the turbulent field is almost 'blind' to the region of positive $\partial \tilde{T}/\partial y$ near the wall and effectively only sees a – compared with adiabatic cases – 'less heated' wall. Turbulence therefore still transports heat away from the wall in the same sense as in adiabatic cases. As a result, both the profiles of the temperature fluctuations in panel (*c* i) and the turbulent heat flux in panel (*c* iii) behave comparably to those of adiabatic cases in panels (*b* i)–(*b* iii); they are only slightly reduced in magnitude, but do not form an additional inner peak in panel (*c* i) or significant negative regions near the wall in panel (*c* iii). Consequently, it is expected that the basic arguments derived for TBLs under adiabatic conditions will still hold reasonably well for TBL cases in the weakly cooled regime, and no substantial modelling problems are expected.

995 A14-16

Referring to figure 1, cases that are indicated as weakly cooled in figure 2(c i–c iii) are located in the *Ec* range of $-0.25 \lessapprox -1/Ec < 0$. Therefore, the value of $-1/Ec \approx -0.25$ is indicated as the dividing line between weakly cooled and moderately cooled cases in figure 1. As will be explained in more detail in § 4.3, this dividing line depends slightly on the local Reynolds number and should therefore only be understood as a guideline for the DNS data shown with rather low Reynolds numbers.

4.2.4. *Moderate cooling conditions*

In moderately cooled TBLs, the temperature peak – and thus the root of $\partial \tilde{T}/\partial y$ – in figure 2(d ii) lies within the buffer layer ($5 \lessapprox y^* \lessapprox 30$) and thus in regions with strong turbulence production. As a result, regions with $\partial \tilde{T}/\partial y > 0$ start affecting the turbulence profiles. In contrast to the lower border of $y^* \approx 5$, the upper border has been defined rather arbitrarily to $y^* \approx 30$, a wall-normal position often defined as the starting point of the logarithmic law of the wall in incompressible flows (Pope 2000). From a physical point of view, this limit was chosen as it roughly coincides with the point at which the inner peak of the $\sqrt{\overline{T'^2}}$ distributions will dominate the outer peak in the panel (d i), a feature that will later be attributed to the regime of strong cooling. Characteristics for the moderately cooled regime are a noticeably negative turbulent heat flux in the region near the wall, see panel (d iii), and a quite characteristic double-peaked structure of the temperature fluctuations with two peaks/plateaus in regions below and above the temperature peak, see panel (d i). Consistently for all plotted data, the root of $\partial \tilde{T}/\partial y$ shifts to larger y^* values as $-1/Ec$ decreases, while the temperature gradient becomes larger near the wall and smaller in the outer region at the same time; similarly, the inner peak of the temperature fluctuations increases and the outer peak decreases. Due to the topological differences compared with adiabatic and weakly cooled cases, modelling issues are to be expected for moderately cooled cases if modelling is solely based on adiabatic arguments.

Referring to figure 1, all cases that are indicated as moderately cooled in figure 2(d i–d iii) are located in the *Ec* range of $-0.45 \lessapprox -1/Ec \lessapprox -0.25$ (where the value of -0.45 stands for $r/2$). However, as for the weakly cooled cases discussed in § 4.2.3, also the wall-normal position of the root of $\partial \tilde{T}/\partial y$ in panel (d ii) shows a noticeable Reynolds-number dependence, compare the red coloured cases. Therefore, also the dividing line between moderately and strongly cooled cases is to be understood as an orientation for the given DNS data only and has to be adapted for higher Reynolds numbers, see also § 4.3.

4.2.5. *Strong cooling conditions*

In strongly cooled TBLs, the temperature peak and thus the root of $\partial \tilde{T}/\partial y$ in figure 2(e ii) lies above the buffer layer $y^* \gtrapprox 30$. For these cases, the thermal quantities are expected to be thoroughly mixed in the outer layer which causes the thermal turbulent field to be dominated by the near-wall regions with $\partial \tilde{T}/\partial y > 0$. The temperature gradient in panel (e ii) is characterized by very steep positive temperature gradients near the wall and only small remaining negative temperature gradients outside. As a result, the temperature fluctuations in panel (e i) are dominated by the inner peak, while the outer peak increasingly vanishes with decreasing $-1/Ec$; the same holds for the turbulent heat flux in panel (e iii). A particular note should be given to the Reynolds-number dependence of the root of $\partial \tilde{T}/\partial y$ in panel (e ii), which is much more pronounced for strongly cooled cases compared with the weakly and moderately cooled regimes discussed before, compare

the two red coloured lines. Since the temperature peak is no longer strictly in the inner layer of the TBL, its wall-normal position scales more with outer scales than with inner scales, leading to a linear outward shift of the temperature-peak position in y^* with increasing Reynolds number, see § 4.3 for details.

Referring to figure 1, the strongly cooled regime is virtually impossible to reach for hypersonic cases as elaborated in § 4.1.1 (at least for low Reynolds numbers, see § 4.3). However, cases such as high-temperature flows with strong cooling at only moderate supersonic speeds, e.g. in rocket nozzles, gas turbines, etc., may well fall into this range due to the large availability of internal energy.

4.2.6. *Quasi-incompressible cooling conditions*

For quasi-incompressible cooling conditions, the cooling at the wall is strong enough that the temperature peak is close to or above the boundary-layer thickness δ_{99}. Since the effect of viscous heating is basically negligible in these conditions, the profiles behave similarly to the incompressible case with $q \approx q_w$. In terms of the Mach number, this regime is only available for lower Mach numbers. As none of the available reference data manage to achieve such a strong cooling, this regime will not be discussed further.

4.3. *Influence of the Reynolds number*

Both from (2.2) and the discussion of figure 2 it is evident that the heat transfer within a boundary layer is not solely influenced by the Eckert number alone, but also – at least to a certain extent – by the local Reynolds number. For instance, the wall-normal position where $\partial \tilde{T}/\partial y = 0$ shifts slightly outwards for cases with a fixed Ec, but increasing Re-number, as shown by the two red lines in figure 2. Consequently, since the strength of how a TBL feels heat transfer increases with Re, a case with a fixed $-1/Ec$ falling within the range of weak cooling at low Reynolds numbers might be shifted to the range of moderate or strong cooling at high Reynolds numbers. Strictly speaking, the (approximate) blue-coloured dividing lines between the individual regimes in figure 1 are therefore only valid for a small-Reynolds-number range, and their success is based primarily on the fact that all DNS data discussed lie in a comparable 'low' range of Re. The objective of this section is therefore to quantify the Reynolds number dependence of the root of $\partial \tilde{T}/\partial y$ – or in other words: the regime bounds in terms of Ec – and to estimate its evolution at larger Reynolds numbers.

4.3.1. *Analytical estimation*

According to Gatski & Bonnet (2013), the velocity at the wall-normal position of the temperature peak ($\partial \tilde{T}/\partial y = 0$) can be approximated by

$$u^+_{\partial \tilde{T}/\partial y=0} = \frac{-B_q}{(\gamma - 1)M_\tau^2}, \tag{4.2}$$

in the inner layer, where $B_q = q_w/(\bar{\rho}_w u_\tau \bar{h}_w)$ and $M_\tau = u_\tau/\bar{a}_w$. To associate (4.2) with Ec, the Ec definition (1.1) is rewritten in terms of B_q and M_τ

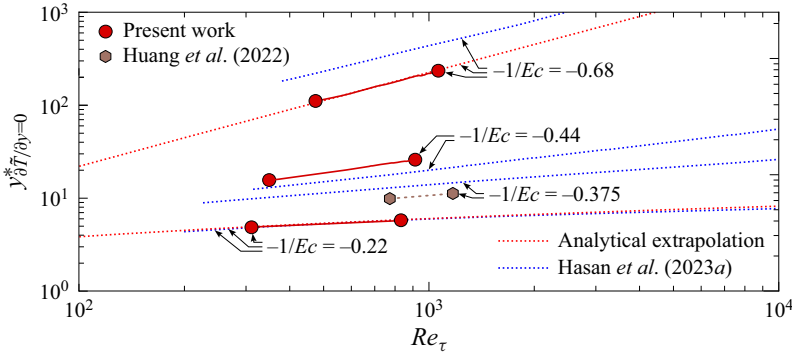$$Ec \approx \frac{M_\tau^2}{B_q} \frac{u_e}{u_\tau}(\gamma - 1)Pr_t, \tag{4.3}$$

Figure 3. Plot of the location of the temperature peak ($\partial \tilde{T}/\partial y = 0$) at $y^*_{\partial \tilde{T}/\partial y=0}$ vs the Reynolds number Re_τ. Shown is the evolution of the DNS data from the present work and Huang *et al.* (2022) compared with the analytical considerations in § 4.3.1 as the red dotted line and the plot in figure 4 based on the tool of Hasan *et al.* (2023*a*) as the blue dotted line.

by utilizing the heat-flux contribution of the SRA $q_w/\tau_w \approx (\bar{T}_w - \bar{T}_r)/Pr_t(c_p/u_e)$, see e.g. Gatski & Bonnet (2013). Combining (4.3) with (4.2) results in

$$u^+_{\partial \tilde{T}/\partial y=0} = -\frac{Pr_t}{Ec}\frac{u_e}{u_\tau} = -\frac{Pr_t}{Ec}\left(\frac{1}{\kappa}\ln(Re_\tau) + c\right), \qquad (4.4)$$

where u_e/u_τ is approximated by $u_e/u_\tau = 1/\kappa \ln(Re_\tau) + c$, see e.g. Panton (2005). Although this expression is an incompressible relation, it is expected to reflect at least the trend of compressible data reasonably well. Based on (4.4) it is straightforward to conclude for weakly cooled cases where $\partial \tilde{T}/\partial y = 0$ is located in the viscous sublayer ($u^+_{\partial \tilde{T}/\partial y=0} = y^+_{\partial \tilde{T}/\partial y=0}$), that the wall-normal position of the temperature peak $y^+_{\partial \tilde{T}/\partial y=0}$ shifts outwards proportional to $\ln(Re_\tau)$; thereby, Pr_t and κ are assumed constant, Ec predefined and c negligible for large Re_τ. Note that this trend perfectly matches the trends observed for the present $-1/Ec = -0.22$ case as depicted in figure 3, if c is calibrated to fit the data. Therefore, the Reynolds-number dependence of the separation line between the weakly and moderately cooled cases in figure 1 is quite robust to changes in Re_τ (especially at high Re_τ), a result that is consistent with the only weak streamwise growth of the viscous sublayer in general.

In the same vein it can be concluded for strongly cooled cases, where $\partial \tilde{T}/\partial y = 0$ is located in the logarithmic layer ($u^+_{\partial \tilde{T}/\partial y=0} = (1/\kappa)\ln(y^+_{\partial \tilde{T}/\partial y=0}) + d$), that $y^+_{\partial \tilde{T}/\partial y=0}$ shifts outwards proportional to Re_τ and thus is influenced quite severely. This expected linear trend is consistent with the observed behaviour of the present $-1/Ec = -0.68$ case as shown in the figure 3, with c and d calibrated to fit the data.

Finally, for cases in the moderately cooled regime where the temperature peak lies within the buffer layer, the Reynolds-number dependence is expected to be somewhere between a logarithmic and a linear evolution, see the present $-1/Ec = -0.44$ case in figure 3.

4.3.2. *Towards a regime diagram including Reynolds-number effects*

To incorporate Reynolds-number influences in the regime diagram, the velocity and temperature profile estimations of Hasan *et al.* (2023*a*) are utilized to estimate the wall-normal position of the temperature peak $y^*_{\partial \tilde{T}/\partial y=0}$ for a wide range of Ec and Re.

Hereby, the velocity profiles are computed using a modified Johnson–King mixing-length eddy-viscosity model and Coles' law of the wake, see Hasan *et al.* (2023*a*) for details. The corresponding temperature profiles are computed from the improved Walz relation of Zhang *et al.* (2014) with $s\,Pr = 0.8$ and $Pr = 0.72$, where s is the Reynolds analogy factor, see e.g. Cogo *et al.* (2023) and Wenzel *et al.* (2021). Note that the profile estimation does not account for high-enthalpy effects as the improved Walz relation by Zhang *et al.* (2014) is applied in temperature formulation. Nevertheless, previous studies (Duan & Martín 2011; Passiatore *et al.* 2022) have shown that the use of a similar enthalpy-based relationship is successful. It is therefore expected that, by using enthalpies to compute $-1/Ec$ or the wall-to-recovery ratios, the current method is also able to provide reasonable estimates under high-enthalpy conditions.

For all subsequent plots, the estimation was solved for specific Ec and Re_τ values and looped between $-0.65 \leqslant -1/Ec \leqslant 0$ and $2 \times 10^2 \leqslant Re_\tau \leqslant 10^5$. The influences of the local Mach number M_e (or M_τ) are assumed to be small, so that all converged cases with different M_e but same Ec and Re_τ were averaged, see § 4.4 for a discussion of this assumption. To improve convergence for strongly cooled cases, minor modifications were made to the initial solutions, such as in the u^+-estimation or the Re_τ-Re_θ relation. Note that the Walz relation directly relates the temperature gradient to the velocity gradient, which makes the estimation of the temperature peak inaccurate for strongly cooled cases where the temperature peak lies in regions of very small velocity gradients. These issues are shared by alternative approaches such as by Huang *et al.* (2023) and Chen *et al.* (2022) which are explicitly not valid in the wake region. In addition, the study by Hasan *et al.* (2023*a*) was strictly speaking only validated for cases with low Reynolds numbers; however, its extrapolation to high Reynolds numbers appears to be a reasonable estimate.

To validate the model under consideration, figure 3 compares the model's prediction of the wall-normal position of the temperature peak $y^*_{\partial\tilde{T}/\partial y=0}$ with those of the present DNS. Essentially, the result confirms the expectation formulated above: the model is quite accurate for weakly cooled cases and becomes increasingly inaccurate for moderately and strongly cooled cases. However, as the general trends are predicted reasonably well, it allows us to extrapolate the Reynolds-number evolution of the heat-transfer regimes introduced for a large parameter space in figure 4. Hereby, all lines depicted indicate constant values of $y^*_{\partial\tilde{T}/\partial y=0}$, while the two red coloured lines with $y^*_{\partial\tilde{T}/\partial y=0} = 5$ and 30 represent the regime boundaries between the weakly, moderately and strongly cooled regimes, respectively. To emphasize that these regime boundaries are by no means abrupt regime changes, but rather transitional regions, these are blurred in blue. Additionally, the minimum possible value for $-1/Ec$ is indicated on the right ordinate for every respective Mach number for the hypothetical case of $\bar{T}_w/\bar{T}_r = 0$, which thus transfers the $\bar{T}_w/\bar{T}_r = 0$ line from figures 1 to 4.

From figure 4 it is noticeable that the Ec range of both the weakly cooled and the moderately cooled regime become significantly smaller with increasing Reynolds number Re_τ. Consequently, in direct agreement with all previous discussions, figure 4 visually underlines the fact that a compressible TBLs at constant $-1/Ec$ feel heat-transfer effects more strongly with increasing Reynolds number Re_τ, as the temperature peak slowly moves outwards. Consequently, a case with constant $-1/Ec$ will gradually move towards a higher cooling regime as Re_τ increases. *Vice versa*, a reduction of the Reynolds number Re_τ implies that some of the proposed regimes are no longer achievable for all Mach- and Reynolds-number combinations. Figure 4 thus visually explains why, with current supercomputing capabilities, most of the recent hypersonic DNS cases with significant
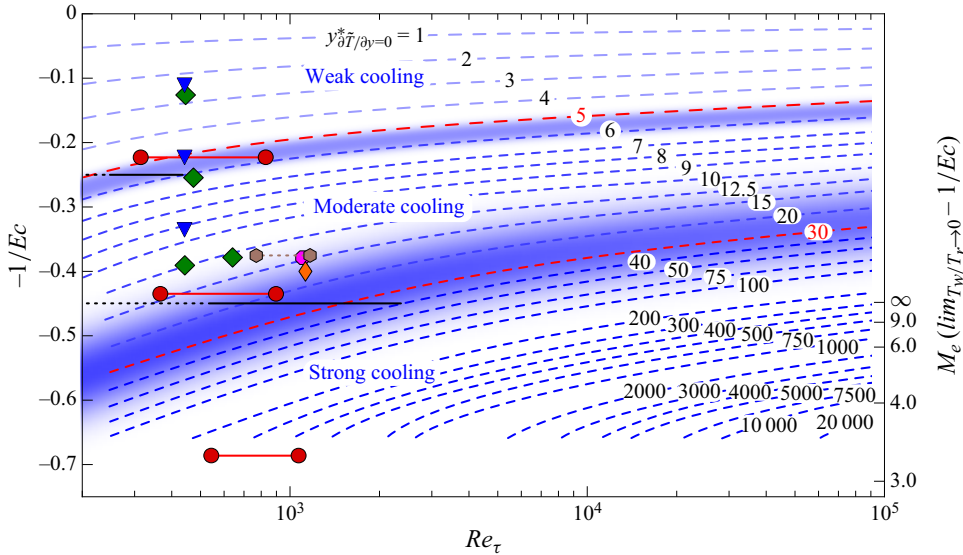
Figure 4. Regime diagram for the cooled cases as $-1/Ec$ over Re_τ. The dashed curved denote the estimated position of $y^*_{\partial \tilde{T}/\partial y=0}$ and the proposed location of the regime change are marked as red curves. The symbols and lines denote the position where the reference data are located in the plot. The two black lines mark the location of the bounds plotted in figure 1 for the DNS data range $400 \lesssim Re_\tau \lesssim 1200$. The right axis marks the Mach number M_e at the equivalent $-1/Ec$ in the limit value $\bar{T}_w/\bar{T}_r \to 0$.

cooling fall 'only' within the moderate cooling range, and why the two-peak structure of temperature fluctuations was not shown in very early low-Reynolds-number DNS.

4.4. *Influence of the Mach number*

So far, the Mach number has been assumed to influence the heat transfer only indirectly by its appearance in the definition of Ec, see (2.2). In reality, however, the Mach number also influences the wall-normal distribution of important thermal variables to a certain extent. These direct Mach-number influences are not captured in the definition of Ec; the purpose of the current section is therefore to estimate to which extent these effects need to be considered in the regime diagram.

4.4.1. *Temperature peak*
As elaborated in § 4.1, the regime diagram introduced is largely based on the wall-normal position of the temperature peak $y^*_{\partial \tilde{T}/\partial y=0}$. Thus, to assess its sensitivity to direct Mach-number influences, $y^*_{\partial \tilde{T}/\partial y=0}$ is evaluated in figure 5(*a*) as a function of M_τ for a constant Re_τ. The data set by Cogo *et al.* (2023) is the only one available that allows for this assessment, as it provides data at various Mach numbers ($2.0 \leqslant M_e \leqslant 6.0$) but equal Ec and Re_τ; these data are depicted as blue coloured symbols in figure 5(*a*) next to the present data in red for reference. From the comparison of cases with the same $-1/Ec$ in figure 5(*a*), $y^*_{\partial \tilde{T}/\partial y=0}$ seems to be virtually unchanged for varying M_τ values. Hence, the wall-normal position of the temperature peak can be assumed to be only slightly influenced by direct Mach-number effects, at least for the parameter range covered by the data set by Cogo *et al.* (2023).
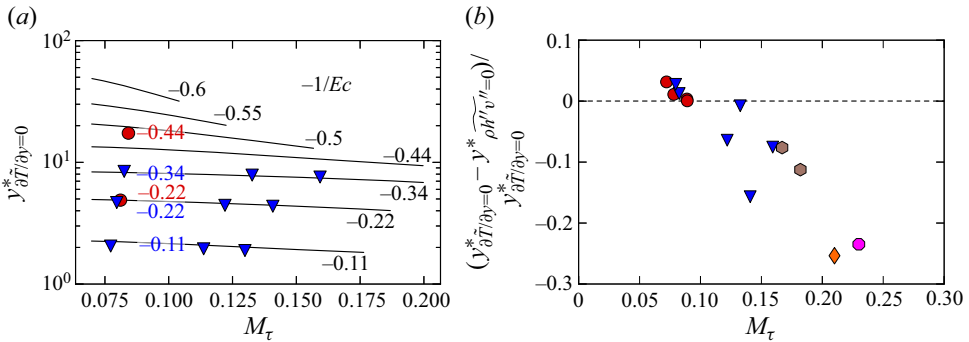
Figure 5. (*a*) Dependence of the location of the temperature maximum $y^*_{\partial\tilde{T}/\partial y=0}$ at $Re_\tau = 443$ on M_τ. (*b*) Relative difference of the temperature maximum $y^*_{\partial\tilde{T}/\partial y=0}$ from the root of the turbulent heat flux $y^*_{\bar{\rho}\widetilde{h''v''}=0}$.

For an extended estimation of direct Mach-number effects across the DNS data towards higher Mach numbers and cooling intensities, figure 5(*a*) shows black-coloured trend lines determined with the profile estimation of Hasan *et al.* (2023*b*,*a*). These data are computed for a unique Reynolds number of $Re_\tau = 443$ and only show the parameter region where convergence of the tool has been achieved. In general, the trend lines show excellent agreement with the DNS data and almost perfectly resemble the slightly decreasing trend for increasing M_τ, as long as $y^*_{\partial\tilde{T}/\partial y=0}$ stays below approximately 10. For higher cooling intensities ($-1/Ec \lesssim -0.4$), the trend lines underestimate the present, red-coloured DNS data with $-1/Ec = -0.44$, see also figure 4, and start to exhibit a much more pronounced M_τ-dependence. Although this trend cannot be confirmed by DNS due to the scarcity of data, the model at least allows us to hypothesize that direct Mach-number influences might have a notable effect on the heat transfer for high–moderate and strongly cooled cases. Note, however, that only a few Mach-number cases will actually be able to reach such low $-1/Ec$-ratios for the comparatively low Reynolds number of $Re_\tau = 443$ chosen. Consequently, more DNS data specially designed to validate this behaviour are sought. A final note refers to the model by Hasan *et al.* (2023*b*) itself, which modifies the van Driest damping constant to compensate for a slight shift of the logarithmic law as function of M_τ. For the present study, the differences between using and not using this model are practically non-existent for the temperature-peak location.

4.4.2. *Relation of the temperature-peak position to the position of $\bar{\rho}\widetilde{h''v''} = 0$*

From figure 2 it is evident that the wall-normal position of the temperature peak ($\partial\tilde{T}/\partial y = 0$ in panels (*c* ii, *d* ii, *e* ii)) and the wall-normal position where the turbulent heat flux becomes zero ($\bar{\rho}\widetilde{h''v''} = 0$ in panels (*c* iii, *d* iii, *e* iii)) differ considerably for cooled cases at high Mach numbers. This mismatch has relevant implications, as $\bar{\rho}\widetilde{h''v''}$ is usually directly associated with $\partial\tilde{T}/\partial y$ in turbulence modelling, an assumption that does not hold for those regions. To characterize the systematics of this trend, the relative distance between $y^*_{\partial\tilde{T}/\partial y=0}$ and $y^*_{\bar{\rho}\widetilde{h''v''}=0}$ with respect to $y^*_{\partial\tilde{T}/\partial y=0}$ is evaluated in figure 5(*b*) as a function of the Mach number M_τ. Only moderately and strongly cooled data are shown, as the direction of the turbulent transport does not change for weakly cooled cases ($\bar{\rho}\widetilde{h''v''} > 0$). As all data points show a fairly consistent trend when plotted over the Mach number M_τ, this mismatch can be approximated at least to the first order as a function of M_τ.

995 A14-22

While this mismatch is fairly small for Mach numbers up to around $M_\tau \approx 0.12$ (which includes the cases to around $M_e \approx 4$), the wall-normal position of $\bar{\rho}\widetilde{h''v''} = 0$ can exceed that of $\partial\tilde{T}/\partial y = 0$ by up to 25 % for the high-enthalpy flows of Di Renzo & Urzay (2021) and Passiatore *et al.* (2022). While the trend appears to be consistent, its practical significance is debatable, as the absolute difference is mostly rather small in cases with large relative differences. In general, this will be the case for most cases as the combination of high M_τ and high wall-normal position of the temperature peak is difficult or impossible to achieve.

4.5. *Influence of high enthalpy*

Some data extracted from TBLs at high enthalpies (Duan & Martín 2011; Di Renzo & Urzay 2021; Passiatore *et al.* 2022) have also been included in figure 1. Before discussing the influence of high enthalpy on the proposed classification, however, the following remarks are made. The regime diagram has been developed taking into account a large collection of low-enthalpy configurations, for which the fluid behaves as a calorically perfect, non-reacting, single-species gas. As discussed in § 2.2.5, high-enthalpy conditions open up new energy transfer pathways that could alter the pictorial representation given by the diagram. A notable example would be the potential presence of a species' thermal diffusion contribution to the wall heat transfer resulting from catalytic or ablative walls, thermal processes *a priori* not covered by the present classification. Moreover, some high-enthalpy effects – such as vibrational excitation and chemical reactions – require the crossing of activation energy thresholds that make their significance depend not only on temperature (or enthalpy) ratios, but also on their absolute values. Lastly, it should be pointed out that vehicles subjected to high stagnation enthalpy conditions are often designed for enhancing heat transfer, because of the need to keep the wall temperature below the creep limits of the surface's material. As a consequence of this engineering constraint, most references consider cooled-wall conditions and the available data fall essentially within the same regime of moderate cooling; the discussion will therefore be mostly limited to such regime. Notwithstanding such limitations, the inclusion of these data allows us to identify how and to which extent high-enthalpy flows can be treated within the present framework, thereby assessing the applicability limits of the regime diagram.

The high-enthalpy data of Di Renzo & Urzay (2021) and Passiatore *et al.* (2022) are shown in panels 2(*d* i)–(*d* iii); note that, for the thermal non-equilibrium case of Passiatore *et al.* (2022), only the rotranslational temperature is reported. Plotted in semi-local units, similar trends are observed with respect to the low-enthalpy configurations within the moderate cooling regime. The wall-normal temperature peak being located in the buffer layer, high-enthalpy phenomena are likely to be most relevant within this flow region, which also corresponds to the area where turbulence activity is the strongest. Owing to the endothermic nature of dissociation reactions and the increase of the fluid's thermal capacity with T, these processes tend to lower $\tilde{T}$ values and therefore also the wall-normal temperature gradient throughout the boundary layer. The reduction of $\partial\tilde{T}/\partial y$, however, is less evident close to the wall and in the outer layer, due to the prescribed T_w and T_e values being lower than the activation temperature for molecular oxygen dissociation. Since the species' production/depletion rates only depend on the local thermodynamic state, the temperature peak's location is not significantly altered. The null gradient position is therefore located in the buffer layer and shows a tendency to be shifted outwards for decreasing $-1/Ec$ values. Note that both data from Di Renzo & Urzay (2021) and Passiatore *et al.* (2022) consider non-catalytic wall conditions, therefore ruling out the effect of gas–surface interactions. The latter can alter the total heat transfer at the wall,

995 A14-23

potentially causing a further shift of the temperature peak towards the log layer. That is the case for the $M_e = 3.4$ configuration considered by Duan & Martín (2011) and reported in figure 1 within the strong cooling regime. Compared with the non-catalytic wall, supercatalytic conditions were shown to move the null gradient location from $y/\delta \approx 0.1$ to ≈ 0.2 (see figure 17 in Duan & Martín 2011). In that case, the catalytic heat-flux contribution is greatly enhanced by the presence of strongly dissociated flow due to the large T_e which, in turn, causes the free stream to be supersonic. On the other hand, when T_e is kept sufficiently low for hypersonic conditions to occur ($M_e = 9.4$ configuration) the $\partial \tilde{T}/\partial y = 0$ locations for the fully and non-catalytic cases are almost superposed, suggesting only a minor influence of the surface's condition. These observations point towards confirming the difficulty of achieving a strong cooling regime at hypersonic speeds, even under high-enthalpy conditions.

With regard to the turbulent heat flux in panel 2(d iii), no substantial deviations are observed for high-enthalpy data. The integral decomposition performed by Li *et al.* (2022) and Liu *et al.* (2023) revealed that the wall-normal species' turbulent transport term consistently keeps negative values throughout the boundary layer; with respect to the temperature-related term, its contribution is negligible in the linear region and becomes of the same order of magnitude from the log layer outwards. This implies that the sign change of $\bar{\rho}\widetilde{h''v''}$ is solely due to the temperature component and justifies the negligible influence observed in § 4.4.2.

When thermal relaxation processes come into play, the longer relaxation times of vibrational modes lead to pronounced deviations of the wall-normal profile of the vibrational temperature ($\tilde{T}_V$) compared with the rotranslational one ($\tilde{T}$). Owing to the sustained vibrational under-excitation within the boundary layer, $\tilde{T}_V$ sensibly decreases and $\overline{T_V'^2}$ loses the characteristic double-peaked structure. The latter, however, should not be considered as a change in the wall cooling regime from the vibrational standpoint, since the $\partial \tilde{T}_V/\partial y = 0$ location is essentially unchanged. Rather, it is a result of the stronger interaction in the buffer layer with turbulence, whose activity tends to smooth out T_V fluctuations. No significant effects are registered on the turbulent heat-flux profile, also because the vibrational component accounts for less than 10 %. Thermal non-equilibrium is stronger close to the turbulence onset; at larger Reynolds numbers, as the flow moves away from this region, its influence decreases and the effects described in § 4.3 are expected to become dominant.

5. Discussion/significance

It was shown in the previous sections that Ec can classify the strength of heat transfer effects to a considerable extent. Further, it was shown that Ec ranges can be identified for which specific characteristics of the thermal flow field occur. It is the aim of this section to work out to what extent some fundamental modelling assumptions, e.g. of the SRA, can be assumed to be approximately valid in the ranges identified or, *vice versa*, are likely to fail. To this end, figure 6 shows a summary of representative quantities that are either the outcome of the classical SRA (Morkovin relations, derived for adiabatic cases, see Morkovin 1962) or the outcome of more advanced SRAs. Note that only our own DNS data are discussed below for overview purposes; however, all conclusions derived are validated with literature data.

First, the wall-normal distribution of the turbulent Prandtl number $Pr_t = (\bar{\rho}\widetilde{v''u''}/\bar{\rho}\widetilde{v''T''})(\partial \tilde{T}/\partial y)/(\partial \bar{u}/\partial y)$ is discussed in outer scaling (y/δ_{99}) in panel (a) and
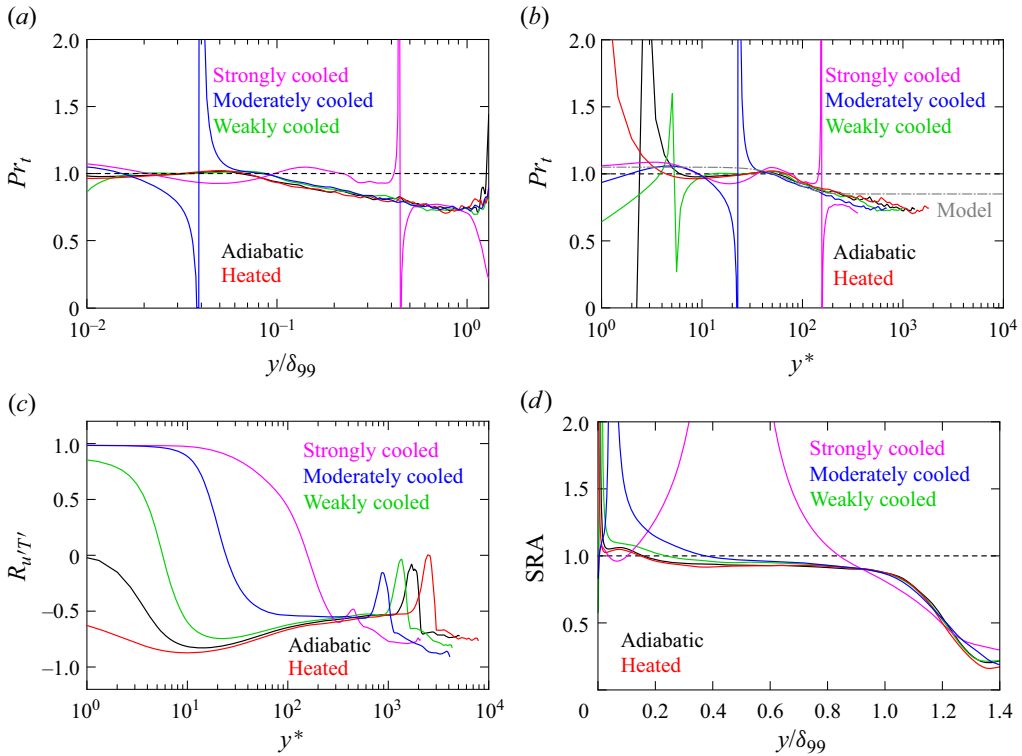
995 A14-24

Figure 6. (*a*) Turbulent Prandtl number over semi-local y^*, (*b*) turbulent Prandtl number over y/δ_{99}, (*c*) the correlation coefficient between T' and u' over the semi-local y^* and (*d*) ratio between (*I*) and (*III*) over y/δ_{99}, verifying (5.1). All plots are evaluated at $Re_\tau = 700$.

semi-local scaling (y^*) in panel (*b*). In various studies, the turbulent Prandtl number has been found to be surprisingly insensitive to the wall-temperature condition and usually shows a falling trend from values of approximately 1 at the wall towards values of approximately 0.75 near the boundary-layer edge. Besides, it is a defining feature for cooled cases that the turbulent Prandtl number exhibits a singularity at the wall-normal position where $\bar\rho \widetilde{v''T''} = 0$, which moves outward as cooling increases. Note that the systematics of how Pr_t approaches the singularity are closely related to the mismatch of $\partial \tilde{T}/\partial y = 0$ and $\bar\rho \widetilde{h''v''} = 0$ discussed in §4.4.2. For all cooled cases except for the strongly cooled case in panel (*a*), this singularity is close to the wall in the low buffer layer or even the viscous sublayer. Note that increasing the cooling intensity for adiabatic to moderately cooled cases has virtually no influence on the wall-normal distribution of Pr_t, which is almost identical for these cases above the singularity. For the strongly cooled case, in contrast, the value of Pr_t is almost identical to the prediction made by the classical SRA of $Pr_t = 1$ (Morkovin 1962) below the singularity for approximately 40 % of the boundary-layer thickness, and thus severely differs from the other cases; above the singularity, the distribution perfectly matches that of all other cases. It is interesting to note that this mismatch seems to be almost completely eliminated in the semi-local scaling in panel (*b*), where all cases show a highly comparable trend that is well captured by e.g. the Pr_t relation by Huang *et al.* (2023) ($Pr_t = 1.05 - 0.2 \tanh^3(y^*/A^*)$ with $A^* = 70$). Thus, panels (*a*,*b*) give evidence that, for strongly cooled cases, the choice of a suitable
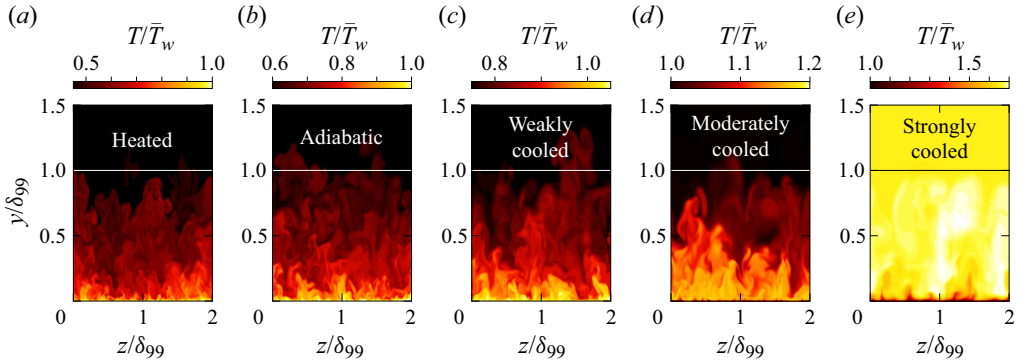
Figure 7. Instantaneous temperature fields $T/\bar{T}_w$ at $Re_\tau = 700$ for the (*a*) heated, (*b*) adiabatic, (*c*) weakly cooled, (*d*) moderately cooled and (*e*) strongly cooled cases.

Pr_t relation is more relevant than for weakly or moderately cooled cases. For the present strongly cooled case, for example, a y/δ_{99}-based model will be significantly misleading for almost 40 % of the boundary layer, while a y^*-based model turns out to be more universal and reliable.

Next, the correlation coefficient $R_{u'T'} = \overline{u'T'}/(\sqrt{\overline{u'^2}}\sqrt{\overline{T'^2}})$ between the velocity and temperature fluctuations u' and T' is plotted in panel (*c*) in semi-local wall-normal units y^*. This quantity intuitively allows us to assess the interplay between velocity and temperature fluctuations. Starting from the far field, all heat-transfer conditions lead to the well-known correlation coefficient of $R_{u'T'} \approx -0.6$ reported in, e.g. Guarini *et al.* (2000) and Pirozzoli *et al.* (2004). However, when moving towards the wall, the correlation coefficient moves to $R_{u'T'} \approx 1$ due to the change in the temperature gradient for increased cooling strength, see also Duan & Martín (2011). Thus, panel (*c*) illustrates the significance of the positive temperature gradient regions near the wall, which – especially for the strongly cooled case – dominate large parts of the boundary layer near the wall. It is a major achievement of the more recent formulations of the SRA like the generalized SRA (Zhang *et al.* 2014), for instance,

$$\underbrace{\sqrt{\overline{T'^2}}}_{(I)} = \underbrace{\left| \frac{1}{Pr_t} \frac{\partial \bar{T}}{\partial \bar{u}} \right| \sqrt{\overline{u'^2}}}_{(II)} = \underbrace{\pm \frac{\bar{\rho}\widetilde{v''T''}}{\bar{\rho}\widetilde{v''u''}} \sqrt{\overline{u'^2}}}_{(III)}, \tag{5.1}$$

that those positive temperature gradient regions in non-adiabatic cases can be incorporated also for the relationships between the temperature fluctuations and the streamwise velocity fluctuations, which essentially constitute the spirit of the SRA. Evaluating the ratio between terms (I) and (III) in panel (*d*) (equivalent to the ratio of (I) and (II)) shows that (5.1) holds remarkably well for large regions of the boundary layer. For regions where $\bar{\rho}\widetilde{v''T''} \approx 0$ or $\partial \bar{T}/\partial \bar{u} \approx 0$, (5.1) predicts $\sqrt{\overline{T'^2}} \approx 0$, resulting in a singularity in panel (*d*) for real flow data. For the strongly cooled case, this region extents over almost the entire boundary-layer thickness, which would predict the temperature fluctuations to be near zero for large regions of the boundary layer. Essentially, this prediction is qualitatively sound, as the temperature fluctuations are indeed small over most of the boundary layer in this case, see figure 7. However, as shown by a comparison with figure 2(*e* i), the temperature fluctuations for the strongly cooled case never actually become zero. Among others, this discrepancy between the prediction by the SRA and the DNS data can be attributed to

995 A14-26

limiting assumptions in the derivation of the SRA such as the parallel flow assumption or the assumption of weak turbulence. However, it is worth noting that this inaccuracy only makes the relative error of (5.1) appear large for strongly cooled cases, while the absolute error is acceptable for most practical applications.

In summary, all previously discussed modelling quantities demonstrate that a variety of modelling approaches already exist today that allow an excellent prediction of the thermal flow field over the entire Ec range. In this context, it is a key value of the regime diagram that an *a priori* estimate can be made of which models should be used for a particular case and how large the expected uncertainties are, if Ec and Re are known.

6. Summary and conclusion

In this study the heat-transfer effects arising from the interplay of Mach number (viscous heating) and wall heat transfer are classified in a regime diagram. To this end, the characteristics of temperature-field-related quantities are considered for both existing and newly computed DNS data within a wide range of Mach numbers and wall-temperature conditions, thereby founding the conclusions on a broad basis. It is shown that the effect of heat transfer can be classified based on the wall-normal position of the temperature peak arising for cooled cases, which separates regions of positive $\partial \tilde{T}/\partial y$ near the wall from regions of negative $\partial \tilde{T}/\partial y$ above. Since the temperature peak shifts further away from the wall with increased cooling strength, the interaction between regions having positive $\partial \tilde{T}/\partial y$ and boundary-layer turbulence is greatly enhanced. The temperature peak is therefore a determining factor for the topological characterization of diabatic boundary layers. In order to have predictive capability the regime diagram is related to the Eckert number Ec (more precisely $-1/Ec$) and the local Reynolds number Re_τ. While the Eckert number has been shown to well characterize heat-transfer effects on most important temperature-related quantities for a wide range of Mach numbers and $\bar{T}_w/\bar{T}_r$ conditions, also the local Reynolds number Re_τ has been shown to affect the strength of heat-transfer effects. Its influence has been quantified for the DNS data under consideration, and estimated at higher Reynolds numbers. Since both Ec and Re_τ can be determined in advance – or estimated to a reasonable extent, it is a key advantage of the classification scheme to allow an effective estimation of to what extent heat-transfer effects are to be expected for the compressible turbulent boundary layer in question. Furthermore, it enables a well-founded prediction of how well different modelling approaches, like the SRA, are suited to a particular boundary-layer case, or whether they need to be replaced by more suitable ones.

More precisely, the regimes introduced are specified as follows:

Heated:	No topological differences are present in the temperature profile compared with adiabatic cases, hence, the heat-transfer strength is characterized solely according to $-1/Ec$ and Re_τ.
Adiabatic:	All cases with $\partial \tilde{T}/\partial y = 0$ at the wall.
Weakly cooled:	A temperature peak $\partial \tilde{T}/\partial y = 0$ is located in the viscous sublayer. Thus, the turbulent thermal field is only barely influenced by the near-wall region with $\partial \tilde{T}/\partial y > 0$, leading to great similarities compared with adiabatic cases. Here, $\sqrt{\overline{T'^2}}$ shows almost no near-wall peak and $\bar{\rho}\widetilde{v''h''}$ is only very weakly negative near the wall (if at all).

Moderately cooled:	The temperature peak $\partial \tilde{T}/\partial y = 0$ is located in the buffer-layer region, causing the near-wall regions with $\partial \tilde{T}/\partial y > 0$ to strongly affect the thermal turbulent field. Here, $\sqrt{\widetilde{T'^2}}$ shows a pronounced near-wall peak and $\bar{\rho}\widetilde{v''h''}$ is clearly negative near the wall.
Strongly cooled:	The temperature peak $\partial \tilde{T}/\partial y = 0$ is located in the log layer or within the wake. Thus, the thermal turbulent field is dominated by regions of $\partial \tilde{T}/\partial y > 0$. Consequently, $\sqrt{\widetilde{T'^2}}$ is dominated by the near-wall inner peak, $\bar{\rho}\widetilde{v''h''}$ by the near-wall negative region.
Quasi-incompressibly cooled:	The temperature peak $\partial \tilde{T}/\partial y = 0$ is close to or above the boundary-layer thickness. The outer peak of $\sqrt{\widetilde{T'^2}}$ has almost completely vanished, $\bar{\rho}\widetilde{v''h''}$ is almost completely negative.

For the considered super- and hypersonic DNS data at approximately $400 \lesssim Re_\tau \lesssim 1200$, the borders between weakly/moderately and moderately/strongly cooled regimes are located at approximately $-1/Ec \approx -0.25$ and -0.45, respectively; most of today's DNS data are thus located in the weakly and moderately cooled regime. However, it should be explicitly noted that the distinction between cooled cases, in particular between moderate and strong cooling, should be regarded as a fluent transition rather than a sharp dividing line.

Further conclusions that can be drawn from the regime diagram are:

Eckert-number effects: both an increase in heating and cooling (increase or decrease in $\bar{T}_w/\bar{T}_r$) and a decrease in M_e result in heat-transfer effects being more pronounced in the wall-normal profiles of temperature-related quantities, since both influences are combined in the Eckert number (see also Wenzel *et al.* 2022). Consequently, with increasing Mach number M_e, an increasingly strong heating or cooling $(\bar{T}_r - \bar{T}_w)$ is necessary to actually achieve strong heat-transfer effects. In addition, the influence of M_e on heat-transfer effects decreases drastically for high hypersonic Mach numbers, leaving the heat transfer almost exclusively a function of $\bar{T}_w/\bar{T}_r$ only. In the case of wall cooling, strong heat-transfer effects already occur at comparatively high $\bar{T}_w/\bar{T}_r$ at low supersonic Mach numbers, and only at extremely low $\bar{T}_w/\bar{T}_r$ values at high supersonic Mach numbers.

Reynolds-number effects: as the wall-normal position of the inner-scaled temperature peak shifts outward with increasing Reynolds number, a boundary layer feels heat-transfer effects more severely at high Reynolds numbers compared with low Reynolds numbers. In this sense, low-Reynolds-number cases are much more likely to be classified into the weakly and moderately cooled regime than in the strongly cooled regime. *Vice versa*, for hypersonic flows, where strong cooling is virtually impossible to achieve for low Reynolds number, this regime becomes accessible for higher Reynolds numbers. Furthermore, it is noted that Reynolds-number effects become stronger the further the temperature peak shifts away from the wall, i.e. the stronger heat-transfer effects become.

Mach-number effects: in addition to 'passive' Mach-number effects, which are already implicitly taken into by the definition of Ec, 'direct' Mach-number effects were shown to affect the regime diagram only very weakly. More precisely, the wall-normal position of

the temperature peak was found to be rather insensitive to a change in the Mach number M_τ, at least for cases with weak or moderate cooling.

High-enthalpy effects: albeit designed on the basis of low-enthalpy flows, the regime diagram is shown to be quite robust with respect to the introduction of high-enthalpy effects. Vibrational excitation and chemical reactions modulate the magnitude of thermal-related quantities, but the wall-normal locations of their critical points are essentially unchanged. For thermal non-equilibrium conditions, the behaviour of the rotranslational modes closely follows the trends observed in low-enthalpy configurations. Owing to their additional heat-flux contribution, catalytic processes can favour stronger cooling regimes when acting in highly dissociated environments, still at the expense of a decrease in the Mach number and a transition from hyper- to supersonic conditions, as predicted by the diagram. Whether a combination of these effects can actually allow to achieve a strongly cooled regime at hypersonic speeds needs therefore further investigation.

Author ORCIDs.
- Tobias Gibis https://orcid.org/0000-0001-9281-4279;
- Luca Sciacovelli https://orcid.org/0000-0002-2463-4193;
- Markus Kloker https://orcid.org/0000-0002-5352-7442;
- Christoph Wenzel https://orcid.org/0000-0002-2526-952X.

Appendix A. Inner scaling

For reference, figure 8 shows the plots of figure 2 in wall units.

Appendix B. Validation of the DNS

In this section a brief description of the validation process of all newly computed DNS cases is given. To this end, figure 9 shows a selection of turbulent quantities at $Re_\tau = 580$ together with the adiabatic reference by Pirozzoli & Bernardini (2011) at $M_e = 2.0$; furthermore, the outer part of the streamwise velocity fluctuation of the weakly cooled case is compared in figure 10(a) with its equivalent reference by Cogo *et al.* (2023) at $Re_\tau = 443$, where no data are available at $Re_\tau = 580$. Both from figures 9 and 10(a) the adiabatic and weakly cooled cases show an overall good match with their equivalent reference data. Differences are mainly the result of the different inlet condition employed (digital filtering vs recycling) and are well in the range of known uncertainties, see e.g. Ceci *et al.* (2022). Since also the moderately cooled case, for which no equivalent reference is available, follows the trend of the other literature data in figure 2, we consider the adiabatic, weakly cooled and moderately cooled cases as validated. For the heated and strongly cooled cases, in contrast, no reference data are available at all. However, as both cases strictly follow the *Ec* trend of the three previously discussed cases in figure 9, both data sets can be considered to be at least plausible. To further enhance reliability of especially the strongly cooled case – which plays a prominent role in this work as
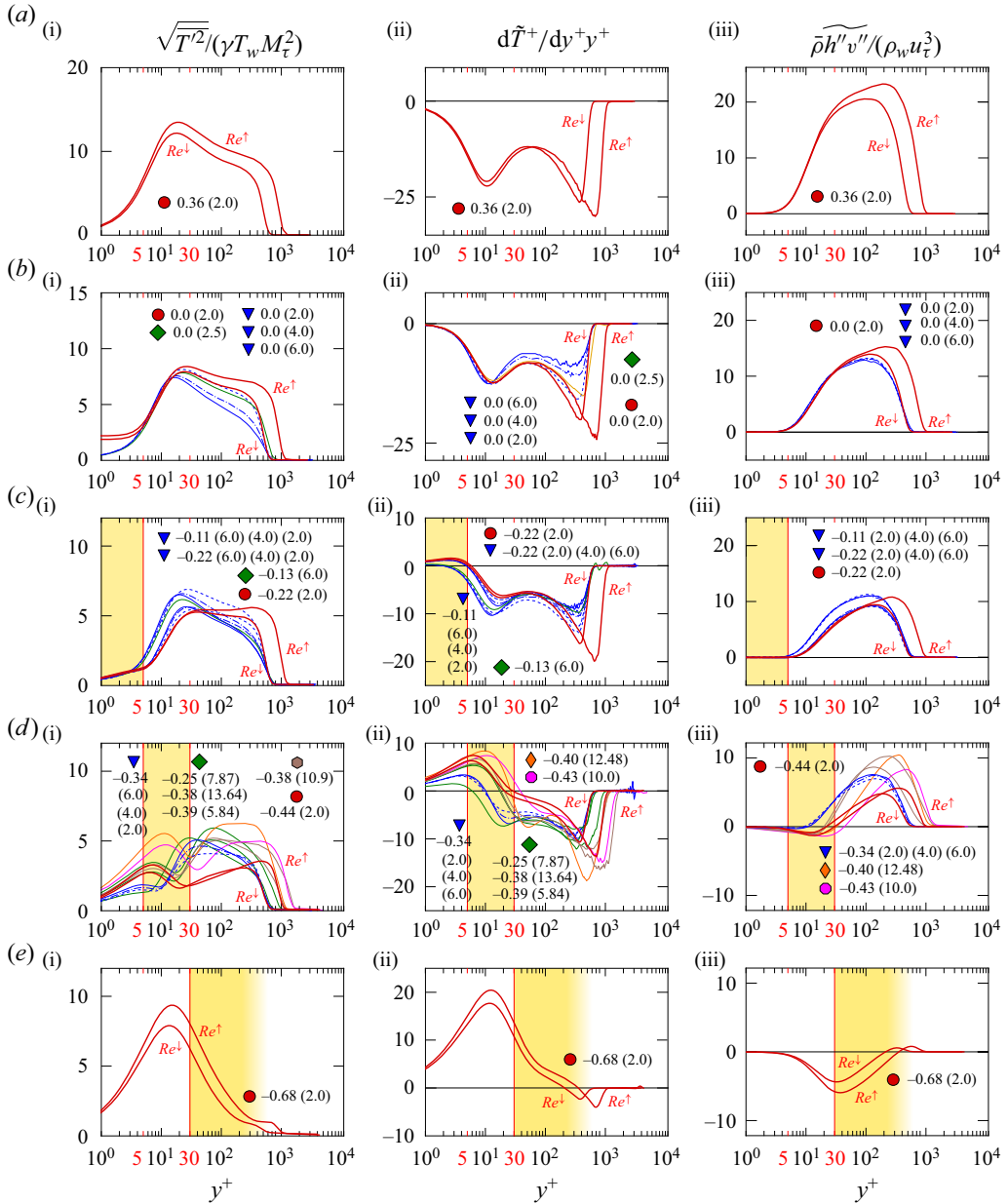
Figure 8. Plot of the inner-scaled temperature fluctuation (labelled as (i) in the left column), the pre-multiplied temperature gradient (labelled as (ii) in the middle column) and the normalized turbulent heat flux (labelled as (iii) in the right column). The rows, from top to bottom, correspond to the regimes: (*a*) heated, (*b*) adiabatic, (*c*) weakly cooled, (*d*) moderately cooled and (*e*) strongly cooled. Each data point is identified by its respective value of $-1/Ec$ and Mach number in brackets (M_e). The legend in figure 1 includes the references for the line colours and symbols.

it was performed at a uniquely low value of $-1/Ec$ – figure 10(*a*,*b*) provides a grid convergence study at three grid resolutions: (i) the present fine grid used for the study (ii) a coarse grid where the resolution in *x* is reduced by a factor of 2, *y* by 1.33 and *z* by 1.5 (iii) and a very fine grid where the resolution in *x* and *z* is increased by a factor of
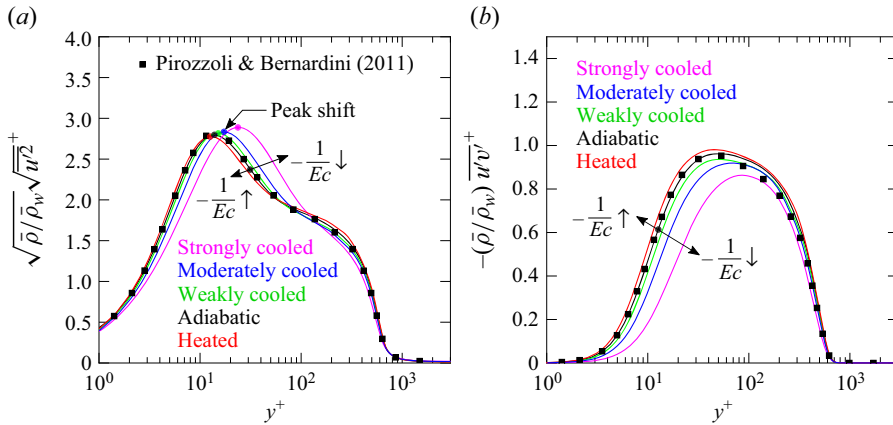
995 A14-30

Figure 9. Fluctuating velocity components in inner scaling at $Re_\tau = 580$. For reference, the adiabatic case of Pirozzoli & Bernardini (2011) is shown as black squares. (*a*) Inner-scaled root mean square of the streamwise velocity. (*b*) Inner-scaled $\overline{u'v'}$ Reynolds stress.
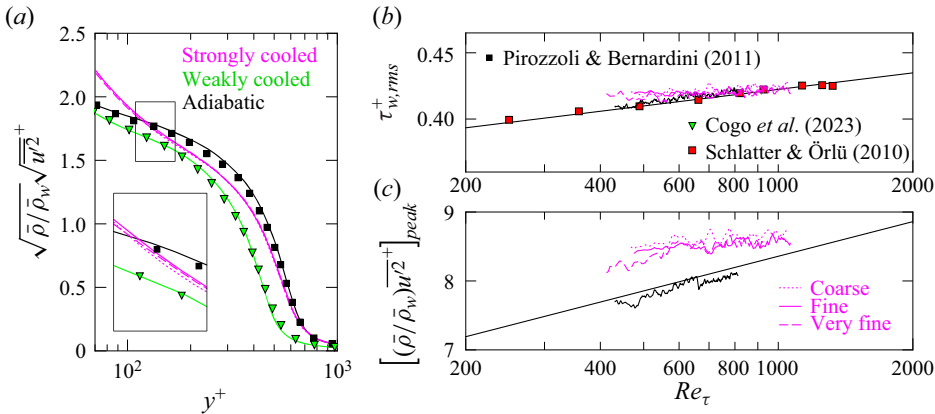

Figure 10. (*a*) Inner-scaled root mean square of the streamwise velocity fluctuation. The adiabatic case is plotted in comparison with Pirozzoli & Bernardini (2011) (black squares) at $Re_\tau = 580$. The weakly cooled case is plotted in comparison with Cogo *et al.* (2023) (green triangles) at $Re_\tau = 443$. The strongly cooled case is plotted in three resolutions at $Re_\tau = 580$. (*b*) Wall shear stress fluctuations over Re_τ with red squares and incompressible trend line from Schlatter & Örlü (2010). (*c*) Peak value of the fluctuating streamwise velocity component with adiabatic $M_e = 2.0$ trend line from Ceci *et al.* (2022).

1.3, while the y resolution is identical. To evaluate grid convergence, figure 10(*a*) depicts the turbulent velocity fluctuation $\sqrt{\overline{u'^2}}^+$ in the outer layer (some reference data are only available in Reynolds averaging), a quantity sensitive to poor grid resolution in this region. Besides, the root mean square of the turbulent wall shear stress $\tau_{w,rms}^+ = \sqrt{\overline{\tau_w'^2}}/\bar{\tau}_w$ and the density-scaled $\overline{u'^2}^+$-peak value over Re_τ are depicted in panels (*b*,*c*), respectively, see also table 4 for a summary of resulting parameters. Overall, all results suggest an already grid-converged state for the coarse grid, which simply results from the fact that, for strongly cooled cases, the effective grid resolution above the viscous sublayer is already drastically increased compared with the nominal grid resolution at the wall because the density has become significantly smaller and the viscosity larger. A minimal grid influence

Case	Δx^+	Δy_w^+	Δz^+	$c_f \times 1000$	H
$cZPG_{sc}$ Coarse	10.4	0.46	9.24	4.162	1.524
$cZPG_{sc}$ Fine	5.19	0.34	4.62	4.166	1.523
$cZPG_{sc}$ Very Fine	3.94	0.35	3.54	4.167	1.523

Table 4. Grid resolution analysis for the strongly cooled case $cZPG_{sc}$ at $Re_\tau = 580$. Given parameters are the resulting grid resolutions Δx^+, Δy_w^+ and Δz^+ in the streamwise, wall-normal and spanwise directions, respectively, as well as the skin-friction coefficient c_f and the shape factor H.

can only be seen for the peak value in panel (*c*), which is marginally higher for the strongly cooled range than for adiabatic cases, see also figure 9(*a*).

REFERENCES

BABUCKE, A. 2009 *Direct Numerical Simulation of Noise-Generation Mechanisms in the Mixing Layer of a Jet*. Verlag Dr. Hut.

BRADSHAW, P. & HUANG, G.P. 1995 The law of the wall in turbulent flow. *Proc. R. Soc. Lond.* A **451** (1941), 165–188.

CANDLER, G. 2019 Rate effects in hypersonic flows. *Annu. Rev. Fluid Mech.* **51** (1), 379–402.

CECI, A., PALUMBO, A., LARSSON, J. & PIROZZOLI, S. 2022 Numerical tripping of high-speed turbulent boundary layers. *Theor. Comput. Fluid Dyn.* **36** (6), 865–886.

CHEN, P.E.S., HUANG, G.P., SHI, Y., YANG, X.I.A. & LV, Y. 2022 A unified temperature transformation for high-Mach-number flows above adiabatic and isothermal walls. *J. Fluid Mech.* **951**, A38.

CHU, Y.-B., ZHUANG, Y.-Q. & LU, X.-Y. 2013 Effect of wall temperature on hypersonic turbulent boundary layer. *J. Turbul.* **14** (12), 37–57.

COGO, M., BAÙ, U., CHINAPPI, M., BERNARDINI, M. & PICANO, F. 2023 Assessment of heat transfer and Mach number effects on high-speed turbulent boundary layers. *J. Fluid Mech.* **974**, A10.

COGO, M., SALVADORE, F., PICANO, F. & BERNARDINI, M. 2022 Direct numerical simulation of supersonic and hypersonic turbulent boundary layers at moderate-high Reynolds numbers and isothermal wall condition. *J. Fluid Mech.* **945**, A30.

DI RENZO, M. & URZAY, J. 2021 Direct numerical simulation of a hypersonic transitional boundary layer at suborbital enthalpies. *J. Fluid Mech.* **912**, A29.

DUAN, L., BEEKMAN, I. & MARTÍN, M.P. 2010 Direct numerical simulation of hypersonic turbulent boundary layers. Part 2. Effect of wall temperature. *J. Fluid Mech.* **655**, 419–445.

DUAN, L. & MARTÍN, M.P. 2011 Direct numerical simulation of hypersonic turbulent boundary layers. Part 4. Effect of high enthalpy. *J. Fluid Mech.* **684**, 25–59.

FERNHOLZ, H.-H., FINLEY, P.J. & MIKULLA, V. 1981 A further compilation of compressible boundary layer data with a survey of turbulence data. *Tech. Rep.* 263. Advisory Group for Aerospace Research and Development Neuilly-Sur-Seine (France).

GATSKI, T.B. & BONNET, J.-P. 2013 *Compressibility, Turbulence and High Speed Flow*. Academic.

GAVIGLIO, J. 1987 Reynolds analogies and experimental study of heat transfer in the supersonic boundary layer. *Intl J. Heat Mass Transfer* **30** (5), 911–926.

GIBIS, T., WENZEL, C., KLOKER, M. & RIST, U. 2019 Self-similar compressible turbulent boundary layers with pressure gradients. Part 2. Self-similarity analysis of the outer layer. *J. Fluid Mech.* **880**, 284–325.

GRIFFIN, K.P., FU, L. & MOIN, P. 2021 Velocity transformation for compressible wall-bounded turbulent flows with and without heat transfer. *Proc. Natl Acad. Sci. USA* **118** (34), e2111144118.

GUARINI, S.E., MOSER, R.D., SHARIFF, K. & WRAY, A. 2000 Direct numerical simulation of a supersonic turbulent boundary layer at Mach 2.5. *J. Fluid Mech.* **414**, 1–33.

HASAN, A.M., LARSSON, J., PIROZZOLI, S. & PECNIK, R. 2023*a* Estimating mean profiles and fluxes in high-speed turbulent boundary layers using inner/outer-layer scalings. *AIAA J.* **0** (0), 1–6.

HASAN, A.M., LARSSON, J., PIROZZOLI, S. & PECNIK, R. 2023*b* Incorporating intrinsic compressibility effects in velocity transformations for wall-bounded turbulent flows. *Phys. Rev. Fluids* **8** (11), L112601.

HUANG, J., DUAN, L. & CHOUDHARI, M.M. 2022 Direct numerical simulation of hypersonic turbulent boundary layers: effect of spatial evolution and Reynolds number. *J. Fluid Mech.* **937**, A3.

HUANG, P.G., COLEMAN, G.N. & BRADSHAW, P. 1995 Compressible turbulent channel flows: DNS results and modelling. *J. Fluid Mech.* **305**, 185–218.

HUANG, P.G., COLEMAN, G.N., SPALART, P.R. & YANG, X.I.A. 2023 Velocity and temperature scalings leading to compressible laws of the wall. *J. Fluid Mech.* **977**, A49.

KELLER, M. & KLOKER, M.J. 2013 Direct numerical simulations of film cooling in a supersonic boundary-layer flow on massively-parallel supercomputers. In *Sustained Simulation Performance 2013* (ed. M. Resch, W. Bez, E. Focht, H. Kobayashi & Y. Kovalenko), pp. 107–128. Springer.

KLOKER, M.J. 1997 A robust high-resolution split-type compact FD scheme for spatial direct numerical simulation of boundary-layer transition. *Appl. Sci. Res.* **59** (4), 25, 353–377.

LAGHA, M., KIM, J., ELDREDGE, J.D. & ZHONG, X. 2011 A numerical study of compressible turbulent boundary layers. *Phys. Fluids* **23** (1), 015106.

LI, J., YU, M., SUN, D., LIU, P. & YUAN, X. 2022 Wall heat transfer in high-enthalpy hypersonic turbulent boundary layers. *Phys. Fluids* **34** (8), 085102.

LIU, P., LI, J., SU, H., SUN, D., YU, M. & YUAN, X. 2023 Wall temperature effects on wall heat flux in high-enthalpy turbulent boundary layers. *Aerosp. Sci. Technol.* **140**, 108432.

MAEDER, T., ADAMS, N.A. & KLEISER, L. 2001 Direct simulation of turbulent supersonic boundary layers by an extended temporal approach. *J. Fluid Mech.* **429**, 187–216.

MCBRIDE, B., ZEHE, M. & GORDON, S. 2002 NASA Glenn coefficients for calculating thermodynamic properties of individual species. *Tech. Rep.* TP-2002-211556. National Aeronautics and Space Administration, John H. Glenn Research Center, Cleveland, Ohio.

MORINISHI, Y., TAMANO, S. & NAKABAYASHI, K. 2004 Direct numerical simulation of compressible turbulent channel flow between adiabatic and isothermal walls. *J. Fluid Mech.* **502**, 273–308.

MORKOVIN, M.V. 1962 Effects of compressibility on turbulent flows. *Mécanique de la Turbulence* **367**, 380.

PANTON, R.L. 2005 Review of wall turbulence as described by composite expansions. *Appl. Mech. Rev.* **58** (1), 1–36.

PASSIATORE, D., SCIACOVELLI, L., CINNELLA, P. & PASCAZIO, G. 2021 Finite-rate chemistry effects in turbulent hypersonic boundary layers: a direct numerical simulation study. *Phys. Rev. Fluids* **6** (5), 054604.

PASSIATORE, D., SCIACOVELLI, L., CINNELLA, P. & PASCAZIO, G. 2022 Thermochemical non-equilibrium effects in turbulent hypersonic boundary layers. *J. Fluid Mech.* **941**, A21.

PATEL, A., BOERSMA, B.J. & PECNIK, R. 2017 Scalar statistics in variable property turbulent channel flows. *Phys. Rev. Fluids* **2** (8), 084604.

PATEL, A., PEETERS, J.W.R., BOERSMA, B.J. & PECNIK, R. 2015 Semi-local scaling and turbulence modulation in variable property turbulent channel flows. *Phys. Fluids* **27** (9), 095101.

PIROZZOLI, S. & BERNARDINI, M. 2011 Turbulence in supersonic boundary layers at moderate Reynolds number. *J. Fluid Mech.* **688**, 120–168.

PIROZZOLI, S., GRASSO, F. & GATSKI, T.B. 2004 Direct numerical simulation and analysis of a spatially evolving supersonic turbulent boundary layer at $M = 2.25$. *Phys. Fluids* **16** (3), 530–545.

POPE, S.B. 2000 *Turbulent Flows*. Cambridge University Press.

SCHLATTER, P. & ÖRLÜ, R. 2010 Assessment of direct numerical simulation data of turbulent boundary layers. *J. Fluid Mech.* **659**, 116–126.

SHADLOO, M.S., HADJADJ, A. & HUSSAIN, F. 2015 Statistical behavior of supersonic turbulent boundary layers with heat transfer at $M_\infty = 2$. *Intl J. Heat Fluid Flow* **53**, 113–134.

SHAHAB, M.F., LEHNASCH, G., GATSKI, T.B. & COMTE, P. 2011 Statistical characteristics of an isothermal, supersonic developing boundary layer flow from DNS data. *Flow Turbul. Combust.* **86** (3), 369–397.

TAMANO, S. & MORINISHI, Y. 2006 Effect of different thermal wall boundary conditions on compressible turbulent channel flow at $M = 1.5$. *J. Fluid Mech.* **548**, 361–373.

TRETTEL, A. & LARSSON, J. 2016 Mean velocity scaling for compressible wall turbulence with heat transfer. *Phys. Fluids* **28** (2), 026102.

WENZEL, C., GIBIS, T. & KLOKER, M. 2022 About the influences of compressibility, heat transfer and pressure gradients in compressible turbulent boundary layers. *J. Fluid Mech.* **930**, A1.

WENZEL, C., GIBIS, T., KLOKER, M. & RIST, U. 2019 Self-similar compressible turbulent boundary layers with pressure gradients. Part 1. Direct numerical simulation and assessment of Morkovin's hypothesis. *J. Fluid Mech.* **880**, 239–283.

WENZEL, C., GIBIS, T., KLOKER, M. & RIST, U. 2021 Reynolds analogy factor in self-similar compressible turbulent boundary layers with pressure gradients. *J. Fluid Mech.* **907**, R4.

WENZEL, C., SELENT, B., KLOKER, M. & RIST, U. 2018 DNS of compressible turbulent boundary layers and assessment of data/scaling-law quality. *J. Fluid Mech.* **842**, 428–468.

WU, B., BI, W., HUSSAIN, F. & SHE, Z.S. 2017 On the invariant mean velocity profile for compressible turbulent boundary layers. *J. Turbul.* **18** (2), 186–202.

XU, D., WANG, J. & CHEN, S. 2023*a* Reynolds number and wall cooling effects on correlations between the thermodynamic variables in hypersonic turbulent boundary layers. *J. Fluid Mech.* **965**, A4.

XU, D., WANG, J. & CHEN, S. 2023*b* Wall cooling effect on spectra and structures of thermodynamic variables in hypersonic turbulent boundary layers. *J. Fluid Mech.* **974**, A55.

XU, D., WANG, J., WAN, M., YU, C., LI, X. & CHEN, S. 2021*a* Compressibility effect in hypersonic boundary layer with isothermal wall condition. *Phys. Rev. Fluids* **6** (5), 054609.

XU, D., WANG, J., WAN, M., YU, C., LI, X. & CHEN, S. 2021*b* Effect of wall temperature on the kinetic energy transfer in a hypersonic turbulent boundary layer. *J. Fluid Mech.* **929**, A33.

YU, M. & XU, C.-X. 2021 Compressibility effects on hypersonic turbulent channel flow with cold walls. *Phys. Fluids* **33** (7), 075106.

ZHANG, C., DUAN, L. & CHOUDHARI, M.M. 2018 Direct numerical simulation database for supersonic and hypersonic turbulent boundary layers. *AIAA J.* **56** (11), 4297–4311.

ZHANG, Y.-S., BI, W.-T., HUSSAIN, F. & SHE, Z.-S. 2014 A generalized Reynolds analogy for compressible wall-bounded turbulent flows. *J. Fluid Mech.* **739**, 392–420.